Linear and nonlinear Bragg diffraction by electromagnetically induced gratings with $\mathcal{PT}$ symmetry and their active control in a Rydberg atomic gas

Jie Gao,[1] Chao Hang,[1,2,3,*] and Guoxiang Huang[1,2,3]

[1]*State Key Laboratory of Precision Spectroscopy, East China Normal University, Shanghai 200241, China*
[2]*NYU-ECNU Institute of Physics, New York University at Shanghai, Shanghai 200062, China*
[3]*Collaborative Innovation Center of Extreme Optics, Shanxi University, Taiyuan, Shanxi 030006, China*

(Received 23 January 2022; accepted 2 June 2022; published 15 June 2022)

Due to its myriad applications in many fields of science and technology, novel light diffraction from specially designed optical gratings is a subject of great interest. Here, we propose a scheme to realize the linear and nonlinear Bragg diffractions from an electromagnetically induced grating (EIG) with parity-time ($\mathcal{PT}$) symmetry in a cold Rydberg atomic gas, where the Rydberg-Rydberg interaction between atoms are mapped to strong and long-range interaction between photons, characterized by a giant nonlocal Kerr nonlinearity. We show that a probe laser beam with very low light intensity incident upon the $\mathcal{PT}$-symmetric EIG can display distinctive asymmetric diffraction patterns, which can be actively manipulated through tuning the gain-absorption coefficient of the EIG and the input power of the laser beam. We also show that the intensity distribution among different diffraction orders depends significantly on the $\mathcal{PT}$-symmetry property of the EIG and on the magnitude and nonlocality degree of the Kerr nonlinearity. In addition, we demonstrate that such Bragg diffraction patterns can be controlled by an external gradient magnetic field, which provides a different way of diffraction control. The research results reported here are not only useful for understanding the unique properties of linear and nonlinear Bragg diffractions by $\mathcal{PT}$-symmetric gratings but may also be promising for designing optical devices applicable in optical information processing and transmission.

DOI: 10.1103/PhysRevA.105.063511

I. INTRODUCTION

Diffraction, a general characteristic of wave phenomena, occurs if the wavefront of a wave is obstructed when encountering a (either transparent or opaque) barrier, by which the wavefront is altered in amplitude, phase, or both [1]. The study on the diffraction of light waves has a long history and is of great importance due to its tremendous applications in many fields of science and engineering [1–3].

Diffraction gratings, optical elements with periodically varying refractive index, can diffract light into different propagation directions and form various optical patterns. Gratings play important roles in optics because they can be served as beam splitters, beam reflectors, grating spectrometers, etc. [1–3]. Since the diffraction grating made by Rittenhouse [3], many schemes have been proposed to investigate grating diffraction characteristics and applications, including ruled [4], silicon [5,6], holographic [7–11], and metal gratings [12–14].

Early studies on grating diffractions were focused on the linear regime. Freund [15] reported a theoretical and experimental demonstration of nonlinear grating diffraction, where the optical refractive index of gratings depends on the light intensity. In recent years, there has been renewed interest in nonlinear grating diffraction and its applications due to the wide availability for manufacturing gratings, such as periodically poled ferroelectric crystals [16–23].

Due to the finding of electromagnetically induced transparency (EIT) [24], in recent decades, electromagnetically induced gratings (EIGs) based on resonant atomic gases have been suggested [25–38]. In such atomic gratings, the periodically varying refractive index for a probe laser field is generated by using a control laser field with spatial amplitude modulation. Compared with solid gratings, atomic EIGs have many striking features and advantages. For example, they are highly controllable due to the existence of various atomic levels and selection rules, and they possess giant Kerr nonlinearities together with significant suppression of optical absorption due to the interplay of light-atom resonance and EIT effect. These features make EIGs very useful for realizing nonlinear grating diffractions and their active controllability.

On the other hand, optical systems with parity-time ($\mathcal{PT}$) symmetry [39–43] have attracted growing attention, as they provide new possibilities for controlling light beams with various intriguing phenomena. Optical $\mathcal{PT}$ symmetry has been used to explore fascinating Bloch oscillations [44,45], nonreciprocal and unidirectional light propagations [46–48], coherent perfect absorbers [49–52], giant light amplification [53], single-mode photon and phonon lasers [54–57], topological energy transfer and mode switching [58,59], enhanced sensing [60–62], non-Hermitian quantum random walks [63,64], and quantum state tomography [65]. Compared with solid-state materials, atomic gases are more advantageous in realization of $\mathcal{PT}$-symmetric structures due to the

*chang@phy.ecnu.edu.cn

configurable refractive index profiles, leading to active control over the gain, absorption, and Kerr nonlinearities [66,67].

In this paper, we propose a scheme to realize the linear and nonlinear Bragg diffractions by using an EIG with $\mathcal{PT}$ symmetry. The system we consider is a Rydberg atomic gas [68] working under the condition of Rydberg-dressed EIT, where the Rydberg-Rydberg interaction between atoms is mapped to strong and long-range interaction between probe-field photons [69–71]. With such a system, the Kerr nonlinearity of the system becomes nonlocal, and its magnitude can have a giant enhancement [72–74]. We show that the probe field with very low light intensity incident upon the $\mathcal{PT}$-symmetric EIG can acquire distinctive asymmetric diffraction patterns; these patterns can be actively manipulated by tuning the gain-absorption coefficient of the EIG as well as the input power of the probe field.

Moreover, we demonstrate that the intensity distribution of the diffraction among different diffraction orders depends significantly on the $\mathcal{PT}$-symmetry property of the EIG and on the magnitude and nonlocality degree of the Kerr nonlinearity. In addition, such Bragg diffraction patterns can be controlled by using an external gradient magnetic field, which provides a different technique for the diffraction control in the present system. The research results reported here are not only beneficial for understanding the unique properties of nonlinear Bragg diffraction based on $\mathcal{PT}$-symmetric EIGs but also useful for designing optical devices that are promising for applications in optical information processing and transmission.

Before proceeding, we note that the asymmetric diffraction by $\mathcal{PT}$-symmetric EIGs has been reported recently by several authors [75–79]. However, our work is different from theirs, with the reasons given in the following. Firstly, what we consider here is the Bragg diffraction from a $\mathcal{PT}$-symmetric atomic EIG by using a Rydberg atomic gas. With such a system, the intensity distribution of diffraction patterns among different diffraction orders, and hence its symmetry property, can be changed actively through tuning the gain-absorption coefficient of the EIG. Secondly, the nonlocal Kerr nonlinearity contributed from the Rydberg-Rydberg interaction between atoms plays a significant role in the formation of the diffraction patterns. The symmetry of the diffraction pattern can be changed by tuning both the magnitude and nonlocality degree of the Kerr nonlinearity. Thirdly, due to the giant Kerr nonlinearity of the system, the generation power for the nonlinear Bragg diffraction can be made very weak, which is favorable for the formation of diffraction patterns at low light levels. Finally, the magnetic-field manipulation of the diffraction provides a way for controlling diffraction patterns.

The remainder of this paper is arranged as follows. In Sec. II, we describe the theoretical model under study and illustrate how to realize the $\mathcal{PT}$-symmetric EIG potential with a Rydberg atomic gas. In Secs. III and IV, we investigate respectively linear and nonlinear Bragg diffractions when a probe laser beam is incident upon the $\mathcal{PT}$-symmetric EIG; we also discuss in detail how the $\mathcal{PT}$-symmetry property of the EIG and the magnitude and nonlocality degree of the Kerr nonlinearity affect the Bragg diffraction patterns. In Sec. V, we consider the Bragg diffraction when an external gradient magnetic field is applied to the system. Finally, in Sec. VI, we summarize the main results obtained in this paper.

II. PHYSICAL MODEL AND REALIZATION OF $\mathcal{PT}$-SYMMETRIC EIGs

A. Physical model and nonlinear envelope equation

We consider a laser-cooled four-level atomic gas with an inverted Y-type configuration. The electric field interacting with the atomic gas reads $\mathbf{E} = \mathbf{E}_p + \mathbf{E}_c + \mathbf{E}_a$, where $\mathbf{E}_j = \mathbf{e}_j \mathcal{E}_j \exp[i(\mathbf{k}_j \cdot \mathbf{r} - \omega_j t)] + \text{H.c.}$, with $\mathbf{e}_j$ the unit polarization vectors and $\mathcal{E}_j$ the field amplitudes ($j = p, c, a$). A weak probe field of angular frequency ω_p (half Rabi frequency Ω_p and wave vector $\mathbf{k}_p$) couples the transition between levels $|1\rangle$ and $|3\rangle$, a strong control field of angular frequency ω_c (half Rabi frequency Ω_c and wave vector $\mathbf{k}_c$) couples the transition between levels $|2\rangle$ and $|3\rangle$, and a strong assistant field of angular frequency ω_a (half Rabi frequency Ω_a and wave vector $\mathbf{k}_a$) couples the transition between levels $|3\rangle$ and $|4\rangle$. The propagation directions of the laser fields are assumed to be $\mathbf{k}_p = (0, 0, k_p)$, $\mathbf{k}_c = (0, 0, k_c)$, and $\mathbf{k}_a = (0, 0, -k_a)$ for suppressing the residual Doppler effect. For realizing an optical $\mathcal{PT}$ symmetry in the system, we assume that an incoherent population pumping (with pumping rate Γ_{21}) is applied, which couples the two low-lying levels $|1\rangle$ and $|2\rangle$ and hence provides an optical gain to the probe field.

Under the electric-dipole and rotating-wave approximations, the Hamiltonian of the atomic gas including the Rydberg-Rydberg interaction is given by the Hamiltonian $H = \mathcal{N}_a \int d^3 r \mathcal{H}(r, t)$, where $\mathcal{N}_a$ is the density of atomic gas and $\mathcal{H}(r, t) = \sum_{\alpha=1}^{4} \hbar \Delta_\alpha \hat{S}_{\alpha\alpha}(r, t) - \hbar[\Omega_p \hat{S}_{13}(r, t) + \Omega_a \hat{S}_{34}(r, t) + \Omega_c \hat{S}_{23}(r, t) + \text{H.c.}] + \mathcal{N}_a \int d^3 r' \hat{S}_{44}(r', t) \hbar V(r' - r) \hat{S}_{44}(r, t)$ is the Hamiltonian density. Here, $\hat{S}_{\alpha\beta} \equiv |\beta\rangle\langle\alpha| \exp\{i[(k_\beta - k_\alpha)r - (\omega_\beta - \omega_\alpha + \Delta_\beta - \Delta_\alpha)t]\}$ is the transition operator related to the levels $|\alpha\rangle$ and $|\beta\rangle$, satisfying the commutation relation $[\hat{S}_{\alpha\beta}(r, t), \hat{S}_{\mu\nu}(r', t)] = (1/\mathcal{N}_a)\delta(r - r')[\delta_{\alpha\nu} \hat{S}_{\mu\beta}(r', t) - \delta_{\mu\beta} \hat{S}_{\alpha\nu}(r', t)]$, with $\hbar\omega_\alpha$ the eigenenergy of the level $|\alpha\rangle$; $\Delta_2 = \omega_p - \omega_c - (\omega_2 - \omega_1)$, $\Delta_3 = \omega_p - (\omega_3 - \omega_1)$, and $\Delta_4 = (\omega_4 - \omega_1) - \omega_p - \omega_a$ are frequency detunings; $\Omega_p = (\mathbf{e}_p \cdot \mathbf{p}_{31})\mathcal{E}_p/\hbar$, $\Omega_c = (\mathbf{e}_c \cdot \mathbf{p}_{32})\mathcal{E}_c/\hbar$, and $\Omega_a = (\mathbf{e}_a \cdot \mathbf{p}_{43})\mathcal{E}_a/\hbar$ are half Rabi frequencies of the probe, control, and assistant fields, respectively, with $\mathbf{p}_{ij}$ the electric dipole matrix elements associated with the transition $|i\rangle \leftrightarrow |j\rangle$. The last term of the Hamiltonian density is the contribution due to the interaction between two Rydberg atoms, respectively, at positions $\mathbf{r}$ and $\mathbf{r}'$, described by the van der Waals potential $\hbar V(\mathbf{r}' - \mathbf{r})$, with $V(\mathbf{r}' - \mathbf{r}) = C_6/|\mathbf{r}' - \mathbf{r}|^6$ (C_6 is a dispersion coefficient) [79].

The dynamics of the atoms is controlled by the optical Bloch equation:

$$\frac{\partial \rho}{\partial t} = -\frac{i}{\hbar}[\hat{H}, \rho] - \Gamma[\rho], \tag{1}$$

where ρ is the density matrix (DM), with the matrix elements defined by $\rho_{\alpha\beta} \equiv \langle \hat{S}_{\alpha\beta} \rangle$ ($\alpha, \beta = 1$–4) describing the atomic population ($\alpha = \beta$) and coherence ($\alpha \neq \beta$); and Γ is the relaxation matrix, contributed from the spontaneous emission and dephasing. The evolution of the probe field is described by the Maxwell equation, which under the slowly varying

amplitude approximation is given by

$$i\left(\frac{\partial}{\partial z}+\frac{1}{c}\frac{\partial}{\partial t}\right)\Omega_p+\frac{1}{2k_p}\left(\frac{\partial^2}{\partial x^2}+\frac{\partial^2}{\partial y^2}\right)\Omega_p +\kappa_{13}\rho_{31} = 0, \tag{2}$$

with the coupling coefficient $\kappa_{13}\equiv\mathcal{N}_a\omega_p|\mathbf{p}_{13}|^2/(2\epsilon_0 c\hbar)$. The second derivative term with respect to the coordinates x and y in the equation describes the diffraction effect of the probe field during the propagation.

Since the probe field is much weaker than the control and assistant fields, we can employ the perturbation expansion $\Omega_p=\sum_{m=1}^{\infty}\epsilon^m\Omega_p^{(m)}$ and $\rho_{\alpha\beta}=\sum_{n=0}^{\infty}\epsilon^n\rho_{\alpha\beta}^{(n)}$ (here, ϵ is a small parameter $\sim\Omega_p/\Omega_c$) for solving the Bloch-Maxwell (MB) equations order by order. Moreover, in this treatment, we go beyond the commonly used mean-field theory by considering the many-body correlations [80]. With the solution of ρ_{31} exact to the third order (for more details, see the Appendix), we obtain the optical susceptibility of the probe field, given by $\chi_p=\mathcal{N}_\alpha(\mathbf{e}_p\cdot\mathbf{p}_{13})^2\rho_{31}/(\varepsilon_0\hbar\Omega_p)$.

The probe-field susceptibility can be further expressed as $\chi_p=\chi_p^{(1)}+\chi_{p,1}^{(3)}|\mathcal{E}_p|^2+\int d^3\mathbf{r}'\chi_{p,2}^{(3)}(\mathbf{r}'-\mathbf{r})|\mathcal{E}_p(\mathbf{r}')|^2$, with

$$\begin{aligned}
\chi_p^{(1)} &= \frac{\mathcal{N}_\alpha(\mathbf{e}_p\cdot\mathbf{p}_{13})^2}{\varepsilon_0\hbar}\alpha_{31}^{(1)},\\
\chi_{p,1}^{(3)} &= \frac{\mathcal{N}_\alpha(\mathbf{e}_p\cdot\mathbf{p}_{13})^4}{\varepsilon_0\hbar^3 D}\\
&\quad\times\left\{d_{21}d_{41}\left[\alpha_{33}^{(2)}-\alpha_{11}^{(2)}\right]\right.\\
&\quad\left.-d_{41}\Omega_c\alpha_{23}^{(2)}-d_{21}\Omega_a^*\alpha_{43}^{(2)}\right\},\\
\chi_{p,2}^{(3)} &= \frac{\mathcal{N}_\alpha^2(\mathbf{e}_p\cdot\mathbf{p}_{13})^4}{\varepsilon_0\hbar^3}V(\mathbf{r}'-\mathbf{r})\alpha_{4441}^{(3)},
\end{aligned}$$

where the explicit expressions of $\alpha_{31}^{(1)}$, $\alpha_{11}^{(2)}$, $\alpha_{33}^{(2)}$, $\alpha_{23}^{(2)}$, $\alpha_{43}^{(2)}$, and $\alpha_{4441}^{(3)}$ are given in Appendix. Here, $\chi_p^{(1)}$ is the linear optical susceptibility and $\chi_{p,1}^{(3)}$ [$\chi_{p,2}^{(3)}$] is the local (nonlocal) nonlinear optical susceptibility, contributed by the atom-photon (atom-atom) interactions. Given the typical system parameters (given below), the third-order nonlinear susceptibility will be mainly contributed by the Rydberg-Rydberg interaction between atoms [74], with the order of magnitude:

$$\chi_{p,2}^{(3)}\approx 10^{-9}\,\mathrm{m^2\,V^{-2}}. \tag{3}$$

This is more than 10 orders of magnitude larger than that obtained by conventional nonlinear optical materials.

The nonlinear envelope equation of the probe field can also be derived at the third-order approximation. For simplicity, we assume that the spatial extension of the input probe beam along the y and z directions is much larger than the range of Rydberg-Rydberg interaction, which is characterized by the width of the nonlocal response function defined below. Under this assumption, the behavior of the nonlocal optical Kerr nonlinearity in the y and z directions can be taken as a local one. Then the nonlinear envelope equation can be reduced into the following dimensionless form:

$$i\frac{\partial U}{\partial\zeta}+\lambda\frac{\partial^2 U}{\partial\xi^2}+V(\xi)U +\int d\xi' W(\xi'-\xi)|U(\xi',\zeta)|^2U(\xi,\zeta) = 0, \tag{4}$$

where $U=\Omega_p/\Omega_{p0}$ (Ω_{p0} is a typical half Rabi frequency of the probe beam, which is constant and much smaller than the half Rabi frequencies of the control and assistant fields), $\zeta=z/L_{\mathrm{EIG}}$ [L_{EIG} is the EIG thickness in the transverse direction (x direction)], $\lambda=L_{\mathrm{EIG}}/L_{\mathrm{diff}}$ ($L_{\mathrm{diff}}=2k_pw_0^2$ is the characteristic diffraction length, with w_0 the radius of the probe beam), and $(\xi,\xi')=(x,x')/w_0$. In the above equation, the dimensionless linear potential has the form $V(\xi)=-k_p^2w_0^2\chi_p^{(1)}(\xi)$, and the nonlocal nonlinear response function is defined by $W(\xi'-\xi)=-2k_p^3w_0^6\Omega_{p0}^2\iint d\eta d\zeta\,\chi_{p,2}^{(3)}(\xi'-\xi,\eta,\zeta)$, with $\eta=y/w_0$. Note that, in Eq. (4), we have neglected the local Kerr nonlinearity contributed from the photon-atom interactions [having the form $-k_p^2w_0^2\Omega_{p0}^2\chi_{p,1}^{(3)}|U|^2U$]. The reason is that the local Kerr nonlinearity is several orders of magnitude smaller than the nonlocal Kerr nonlinearity [72,80].

To be concrete, we take a cold gas of strontium 87 atoms (^{87}Sr atoms) as a realistic candidate for the realization of the model described above. The assigned atomic levels are $|1\rangle=|5s^2\ {}^1S_0,\ F=9/2,m_F=-\frac{1}{2}\rangle$, $|2\rangle=|5s^2\ {}^1S_0,\ F=\frac{9}{2},m_F=\frac{3}{2}\rangle$, $|3\rangle=|5s5p\ {}^1P_1\rangle$, and $|4\rangle=|5sns\ {}^1S_0\rangle$. The dispersion parameter $C_6\approx 2\pi\times\ 10.9\,\mathrm{GHz}\,\mu\mathrm{m}^6$ for the main quantum number $n=60$ [81]. The incoherent population pumping rate is $\Gamma_{21}\approx 2\pi\times 0.1\,\mathrm{MHz}$, and the spontaneous emission decay rates are $\Gamma_2=\Gamma_{12}\approx 2\pi\times 0.1\,\mathrm{MHz}$, $\Gamma_3=\Gamma_{13}+\Gamma_{23}\approx 2\pi\times 16\,\mathrm{MHz}$ (with $\Gamma_{13}\approx\Gamma_{23}$), and $\Gamma_4=\Gamma_{34}\approx 2\pi\times 16.7\,\mathrm{kHz}$, respectively. The density of the atomic gas $\mathcal{N}_a=1.0\times10^{12}\ \mathrm{cm^{-3}}$ and the frequency detunings $\Delta_2=-1.186$ MHz, $\Delta_3=50$ MHz, and $\Delta_4=-100$ MHz. The half Rabi frequencies of the control and assistant fields are $\Omega_c=15$ MHz and $\Omega_a=10$ MHz, respectively. The wavelength of the probe beam is $\lambda_p=2\pi/k_p\approx 689$ nm. Since $|\Delta_3+\Delta_4|\gg|\Omega_a|$, the system works in the *Rydberg-dressed* regime, i.e., only a small part of the atoms can be excited to the Rydberg state $|4\rangle$.

By using the above parameters and considering that $\Omega_{p0}\approx 0.1$ MHz, we obtain the approximate expression of the nonlinear response function:

$$W(\xi'-\xi)\approx W_0\iint d\eta d\zeta \times\left\{W_1+\frac{\left[(\xi'-\xi)^2+\eta^2+4k_p^2w_0^2\zeta^2\right]^3}{\left(\frac{0.48R_b}{w_0}\right)^6}\right\}^{-1}, \tag{5}$$

with $W_0=0.02$, $W_1=1+i0.41$, and the radius of Rydberg blockade [82] $R_b\approx 5.6\,\mu$m. Note that the nonlinear response function obeys the normalization condition $\int d\xi W(\xi'-\xi)\approx 1$, which is consistent with the local limit $W(\xi'-\xi)=\delta(\xi'-\xi)$. Since W is positive, the nonlocal Kerr nonlinearity in Eq. (4) is *self-focusing*, which is due to the attractive Rydberg-Rydberg interaction (i.e., C_6 is positive) for the selected atoms.

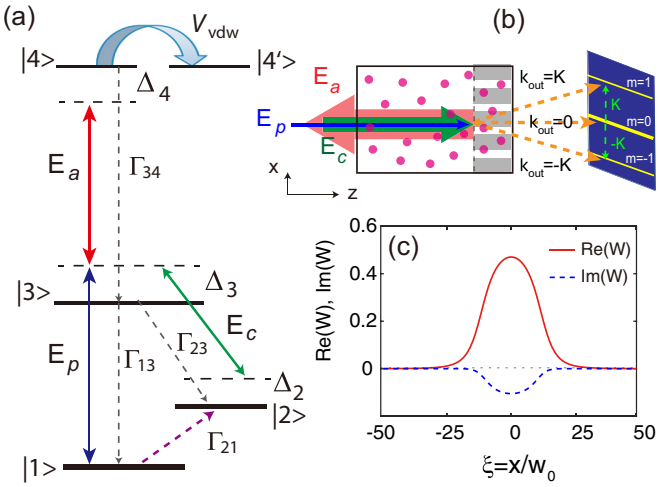

FIG. 1. (a) Level diagram a excitation scheme of the Rydberg-dressed electromagnetically induced transparency (EIT). Energy levels $|1\rangle$, $|2\rangle$, and $|3\rangle$ constitute a Λ-type EIT configuration, where the probe laser field E_p couples the transition $|1\rangle \leftrightarrow |2\rangle$ and the control laser field E_c couples the transition $|2\rangle \leftrightarrow |3\rangle$. Δ_j are detunings, and Γ_{jl} are the spontaneous-emission decay rate from $|l\rangle$ to $|j\rangle$. The Λ-type EIT is dressed by a high-lying Rydberg state $|4\rangle$, which is far-off-resonantly coupled to state $|3\rangle$ through an assistant laser field E_a. An incoherent pumping (with the pumping rate Γ_{21}) is applied to pump the atoms from $|1\rangle$ to $|2\rangle$. The interaction between two Rydberg atoms is described by the van der Waals potential V_{vdw}. (b) Possible setting of Bragg diffraction for the probe beam normally incident on the atomic EIG (denoted by the white and gray region). The cold Rydberg gas is filled in the atomic cell. Projection of the diffracted probe-field wave vector in the x direction can be seen as $k_{out} = mK$ for the mth-order diffraction mode. (c) Spatial distributions of the real and imaginary parts of the nonlinear response function, Re(W) (the red solid line) and Im(W) (the blue dashed line), as functions of $\xi = x/w_0$.

Figure 1(c) shows the spatial distribution of the real and imaginary parts of the nonlinear response function W, i.e., Re(W) and Im(W), as functions of $\xi = x/w_0$. We see that Re(W) $\gg$ Im(W), which means that the optical absorption is largely suppressed. This is contributed by the EIT effect induced by the control field.

B. Realization of $\mathcal{PT}$-symmetric EIGs

Since the present system is highly controllable and can be easily manipulated, it is possible to create an atomic EIG with $\mathcal{PT}$ symmetry by designing the linear optical potential $V(\xi)$ in Eq. (4). To this end, the target potential (i.e., the EIG potential) is set to be a $\mathcal{PT}$-symmetric periodic one with the simple form:

$$V(\xi) = V_0 - V_1 \cos(K\xi) + iV_2 \sin(K\xi), \tag{6}$$

where V_0 is a constant (the constant part of the potential), V_1 (V_2) determines the real (imaginary) part of the potential, and K is the lattice vector (all parameters are dimensionless). Since $V(\xi) = V(-\xi)^*$, the EIG potential is $\mathcal{PT}$ symmetric and the $\mathcal{PT}$ symmetry-breaking point locates at $V_1 = V_2$.

With the parameters of the ^{87}Sr atoms given above, the target potential can be created by the spatially modulated

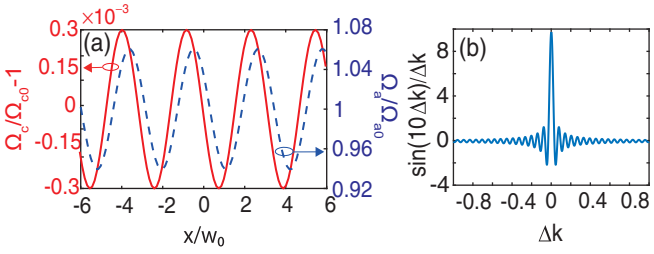

FIG. 2. (a) Spatially modulated half Rabi frequencies of the control and assistant fields, Ω_c/Ω_{c0} (red solid line) and Ω_a/Ω_{a0} (blue dashed line), as functions of $\xi = x/w_0$ for $V_1 = V_2 = 0.01$. (b) The factor $\sin[\Delta k L_{EIG}/(2w_0)]/\Delta k$ as a function of Δk with $\Delta k = mK - k_{diff}$ for $L_{EIG}/(2w_0) = 100$.

control and assistant fields by using the method proposed in Refs. [66,83], reading as

$$\frac{\Omega_c(\xi)}{\Omega_{c0}} = 1 + 0.03V_2 \sin(K\xi), \tag{7a}$$

$$\frac{\Omega_a(\xi)}{\Omega_{a0}} = 1 + 3.44V_1 \cos(K\xi) - 5.02V_2 \sin(K\xi), \tag{7b}$$

with $\Omega_{c0} = 15$ MHz and $\Omega_{a0} = 10$ MHz. From Eqs. (7a) and (7b), we see that Ω_c and Ω_a are now modulated around Ω_{c0} and Ω_{a0}, respectively.

In an experiment, the spatial modulation of the control and assistant fields [Eqs. (7a) and (7b)] can be created simply by using space light modulators. It can also be realized by overlapping the spatial modulation part of the control and assistant fields over their constant part. The spatially modulated control and assistant fields in the form of standing waves can be realized through using pairs of counterpropagating control and assistant beams along the x direction. In addition, the spatial modulation part of the control and assistant fields is shorter than their constant part in the z direction. Thus, the probe beam is incident in the homogenous atomic gas, firstly, without being affected by the EIG potential; then it is incident normally on the EIG potential and diffracts.

Shown in Fig. 2 are the half Rabi frequencies of the control and assistant fields as functions of $\xi = x/w_0$, given by Eq. (7). Here, we have taken $V_1 = V_2 = 0.01$.

III. LINEAR BRAGG DIFFRACTIONS BY $\mathcal{PT}$-SYMMETRIC EIGs

The grating diffractions can be classified in different diffraction regimes. Raman-Nath and Bragg regimes are two conventional ones, which are, respectively, for optical thin and thick media [84]. Different from our earlier work [79], where the Raman-Nath diffraction by a $\mathcal{PT}$-symmetric EIG was considered. Here, we consider the case of Bragg diffraction from the $\mathcal{PT}$-symmetric EIG described in the last section.

We first consider linear Bragg diffraction in the system, which occurs if the input probe beam is very weak (i.e., $|U(\xi, \zeta)| \ll 1$), so that the Kerr nonlinear effect plays no significant role, and hence, the nonlinearity term in Eq. (4) can be neglected. For simplicity, we consider the case that the probe field with a finite transverse width [85] is normally incident to the grating. Then the solution of Eq. (4) takes the form $U(\xi, \zeta) = u(\xi)e^{-i\omega\zeta}$, where the function u satisfies the

inhomogeneous equation:

$$\hat{L}u = -V(\xi)u, \tag{8}$$

with the linear operator $\hat{L} \equiv \omega + \lambda\partial^2/\partial\xi^2$.

Equation (8) can be solved by using Green's function $G(\xi, \xi', \omega)$, satisfying the equation $\hat{L}G(\xi, \xi', \omega) = \delta(\xi - \xi')$, which has the solution:

$$G(\xi, \xi', \omega) = \frac{1}{2\pi}\int_{-\infty}^{\infty} dk\, \frac{\exp[ik(\xi - \xi')]}{\omega - \lambda k^2} = -\frac{1}{4\pi\sqrt{\omega}}\int_{-\infty}^{\infty} dk \times \left\{\frac{\exp[ik(\xi - \xi')]}{\sqrt{\lambda}k - \sqrt{\omega}} - \frac{\exp[ik(\xi - \xi')]}{\sqrt{\lambda}k + \sqrt{\omega}}\right\}. \tag{9}$$

Noting that the integrand in the above integral has two first-order poles located at $k = k_{\pm} \equiv \pm\sqrt{\omega/\lambda}$, one can carry out the integration in Eq. (9) by using the residue theorem, which yields the result:

$$G(\xi, \xi', \omega) = -\frac{i}{2\sqrt{\omega}}\exp\left[i\sqrt{\frac{\omega}{\lambda}}(\xi - \xi')\right]. \tag{10}$$

With this Green's function, Eq. (8) is converted into an integral equation:

$$u(\xi) = u_0\exp(ik_{\rm diff}\xi) - \int d\xi' G(\xi, \xi', \omega)V(\xi')u(\xi'), \tag{11}$$

where the first term on the right-hand side comes from the contribution by the homogeneous equation $\hat{L}u(\xi) = 0$, with u_0 a constant and $k_{\rm diff}$ the diffracted probe-field wave vector, satisfying the relation $\omega = \lambda k_{\rm diff}^2$.

The explicit analytical solution of the integral Eq. (11) can be obtained by employing the Born approximation. Since u is a small quantity, $u(\xi')$ in the integral of Eq. (11) can be replaced by the solution of the zeroth-order approximation [i.e., $u(\xi') = u_0\exp(ik_{\rm diff}\xi')$]. Thus, when exact to the first-order approximation, the solution of Eq. (11) is given by

$$u(\xi) = u_0\exp(ik_{\rm diff}\xi)\left\{1 + \frac{i}{2\sqrt{\omega}}\sum_{m\in\mathbb{Z}} c_m\int d\xi' \times \exp[i(mK - k_{\rm diff})\xi']\right\}. \tag{12}$$

To get this result, we have used the periodic property of the EIG potential $V(\xi)$ and expanded it into a Fourier series, i.e., $V(\xi) = \sum_{m\in\mathbb{Z}} c_m e^{imK\xi'}$. Here, c_m is the expansion coefficient; $m \in \mathbb{Z} \equiv \{0, \pm1, \pm2, \ldots\}$ are integral numbers characterizing the periodicity of the EIG; $K = 2\pi w_0/\Lambda$ is the lattice vector; and Λ is the EIG period along the x direction.

With the result in Eq. (12), in the absence of Kerr nonlinearity, we obtain the solution of Eq. (4):

$$U(\xi, \zeta) = u_0\exp[i(k_{\rm diff}\xi - \omega\zeta)] \times \left\{1 + \frac{i}{2\sqrt{\omega}}\sum_{m\in\mathbb{Z}} c_m \times \int_{-L_{\rm EIG}/(2w_0)}^{L_{\rm EIG}/(2w_0)} d\xi' \exp[i(mK - k_{\rm diff})\xi']\right\}, \tag{13}$$

where $L_{\rm EIG}$ is the EIG thickness in the x direction. Moreover, we have added the lower and upper bounds of the integral which is dependent on the EIG thickness. It is obvious that the dominant contribution to the integral in Eq. (13) comes from the wave numbers mK fulfilling the Bragg diffraction condition:

$$k_{\rm diff} = mK \equiv k_{\rm diff}^m. \tag{14}$$

Since the diffraction wave numbers $k_{\rm diff}^m = k_p\sin\theta_{\rm diff}^m$, here, $k_p = 2\pi/\lambda_p$, and $\theta_{\rm diff}^m$ is the diffraction angle of the mth-order diffraction, the Bragg diffraction condition in Eq. (14) can be written into the well-known form:

$$\sin\theta_{\rm diff}^m = \frac{m\lambda_p}{\Lambda}. \tag{15}$$

When $mK \neq k_{\rm diff}$, after carrying out the integral in Eq. (13), we get

$$U(\xi, \zeta) = u_0\exp[i(k_{\rm diff}\xi - \omega\zeta)] \times \left\{1 + \frac{i}{\sqrt{\omega}}\sum_{m\in\mathbb{Z}} c_m\frac{\sin\left[\frac{(mK - k_{\rm diff})L_{\rm EIG}}{2w_0}\right]}{mK - k_{\rm diff}}\right\}. \tag{16}$$

Note that the factor $\sin[(mK - k_{\rm diff})L_{\rm EIG}/(2w_0)]/(mK - k_{\rm diff})$ is sharply peaked around $mK = k_{\rm diff}$ if $L_{\rm EIG}/w_0 \gg 1$. This means that, to realize a pronounced Bragg diffraction, the EIG thickness $L_{\rm EIG}$ should be much larger than the probe beam radius w_0. Since the occurrence of the Bragg diffraction is due to the interference between the probe beams that are reflected from different layers of the EIG, the EIG must be prepared to be thick enough for making the interference effect significant (i.e., the system works in the regime of Bragg diffraction).

Shown in Fig. 2(b) is the factor $\sin[\Delta k L_{\rm EIG}/(2w_0)]/\Delta k$ as a function of Δk with $\Delta k = mK - k_{\rm diff}$ for $L_{\rm EIG}/(2w_0) = 100$. Since $L_{\rm EIG}/w_0 \gg 1$, the factor is sharply peaked around $\Delta k = 0$, which is exactly the Bragg diffraction condition in Eq. (14).

To confirm that the EIG under study indeed operates in the regime of Bragg diffraction, we fix the radius of the probe beam $w_0 = 20\,\mu$m and the EIG period $\Lambda = 0.2$ mm. These values give the lattice vector $K = 2\pi \times 0.1$ (K is a dimensionless parameter), and the characteristic diffraction length $L_{\rm diff} \approx 7$ mm ($L_{\rm diff}$ is four times larger than the Rayleigh length, given by $\pi w_0^2/\lambda_p \approx 2$ mm, with $\lambda_p \approx 689$ nm). By further selecting the EIG thickness in the x direction $L_{\rm EIG} = 10\Lambda = 2$ mm, we have $L_{\rm EIG}/w_0 = 100 \gg 1$. Thus, the EIG is indeed thick enough in the transverse direction (x direction) so that the Bragg condition in Eq. (15) can be satisfied; meanwhile, the EIG is also long enough in the propagation distance (z direction) which, for instance, can also be taken as 2 mm. Then the interaction region between the probe beam and the EIG is sufficiently large, so that the incident beam can experience multiple scattering by the EIG. Note that, different from Ref. [84], in our situation, the second-order derivative term in the wave equation [i.e., the second term in Eq. (4) for describing the diffraction] cannot be neglected because the coefficient $\lambda = L_{\rm EIG}/L_{\rm diff} \approx 0.3$ is not much less than 1. Due to the finite transverse width of the incident probe beam, the photons in the beam have momentums in the transverse directions. The diffraction angle of the first-order diffraction mode is estimated to be $\theta_{\rm diff}^{\pm1} \approx \pm\lambda_p/\Lambda \approx \pm3.4$ mrad.

To show the spatial distribution (pattern) of the Bragg diffraction from the $\mathcal{PT}$-symmetric EIG, we substitute

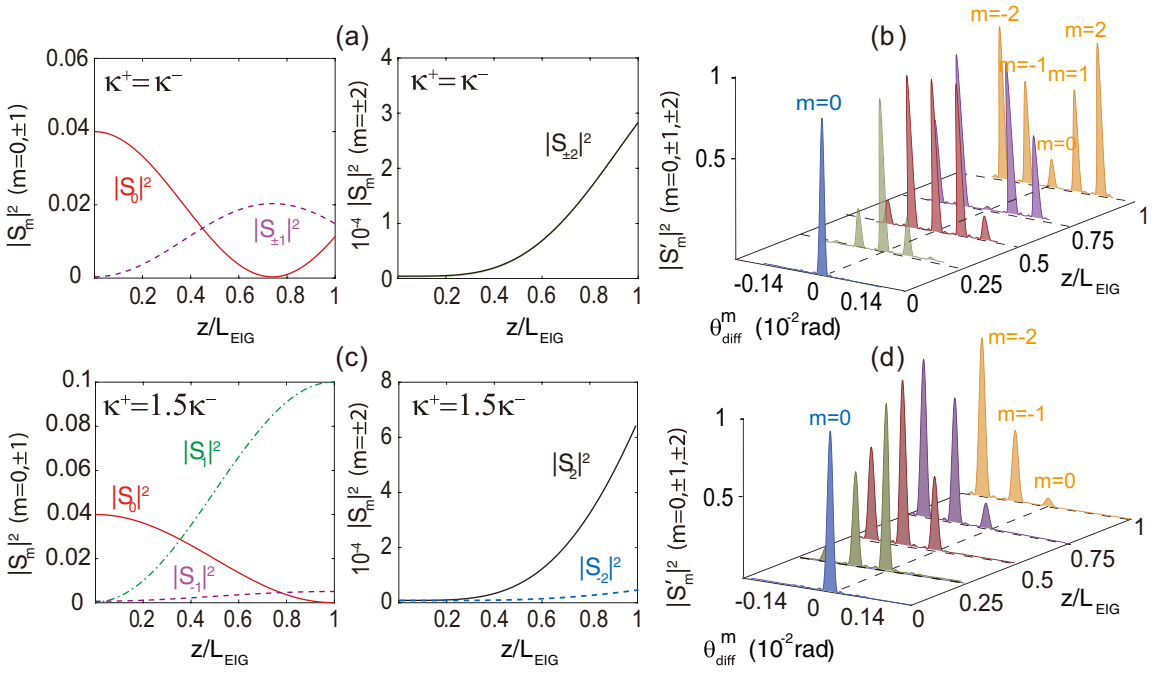

FIG. 3. Intensity distributions of linear Bragg diffraction modes generated by the electromagnetically induced grating (EIG) potential. (a) and (c) Diffraction mode intensities $|S_m(\zeta)|^2$ ($m = 0, \pm1, \pm2$) as functions of $\zeta = z/L_{\rm EIG}$ for $\kappa_+ = \kappa_-$ (real potential) and $\kappa_+ = 1.5\kappa_-$ (complex potential), respectively. (b) and (d) Normalized mode intensities $|S'_m(\zeta)|^2$ (each mode intensity is normalized by its maximum) as functions of the diffraction angle $\theta^m_{\rm diff}$ and $\zeta = z/L_{\rm EIG}$. Symmetric (asymmetric) diffraction emerges in the case of $\kappa_+ = \kappa_-$ ($\kappa_+ = 1.5\kappa_-$). The mode index m is indicated for the mode intensities at $z/L_{\rm EIG} = 0$ and 1.

$k_{\rm diff} = mK$ into Eq. (13), which gives rise to the solution

$$U(\xi,\zeta) = u_0 \exp[i(mK\xi - \omega\zeta)]\left(1 + \frac{i}{2\sqrt{\omega}}\frac{L_{\rm EIG}}{w_0}\sum_{m\in\mathbb{Z}} c_m\right) \equiv S_m(\zeta)\exp(imK\xi), \quad (17)$$

where $S_m(\zeta)$ is the amplitude of the mth-order diffraction mode. Then by substituting Eqs. (17) and (6) into Eq. (4) in the absence of the Kerr nonlinearity, i.e., $i\partial_\zeta U + \lambda\partial_{\xi\xi}U + V(\xi)U = 0$, we attain the equation of motion for the diffraction modes with different diffraction orders:

$$\frac{dS_m(\zeta)}{d\zeta} = i[-\lambda m^2K^2S_m(\zeta) + \kappa_-S_{m+1}(\zeta) + \kappa_+S_{m-1}(\zeta)]. \quad (18)$$

The boundary conditions are given as $S_0(\zeta = 0) = 1$ and $S_m(\zeta = 0) = 0$ ($m \neq 0$). Here, the coupling constants $\kappa_\pm = (V_1 \pm V_2)/2$, which depend on the real and imaginary parts of the EIG potential (i.e., V_1 and V_2). When the EIG potential is real (i.e., $V_2 = 0$), one has $\kappa_+ = \kappa_-$; otherwise, when it is complex (i.e., $V_2 \neq 0$), one has $\kappa_+ \neq \kappa_-$. Since the Bragg diffraction usually includes only a few diffraction orders, we can solve Eq. (18) by keeping terms for $|m| \leqslant 2$, i.e.,

$$\frac{dS_0}{d\zeta} = i(\kappa_+S_{-1} + \kappa_-S_1), \quad (19)$$

$$\frac{dS_{\pm1}}{d\zeta} = i(\kappa_\pm S_0 - \lambda K^2S_{\pm1} + \kappa_\mp S_{\pm2}), \quad (20)$$

$$\frac{dS_{\pm2}}{d\zeta} = i(\kappa_\pm S_{\pm1} - 4\lambda K^2S_{\pm2}). \quad (21)$$

They are solved numerically by using the fourth-order Runge-Kutta algorithm.

Shown in Fig. 3 are the intensity distributions of different diffraction modes generated by the EIG potential, i.e., $|S_m(\zeta)|^2$ ($m = 0, \pm1, \pm2$) as functions of $\zeta = z/L_{\rm EIG}$ for $\kappa_+ = \kappa_-$ [Fig. 3(a)] and $\kappa_+ = 1.5\kappa_-$ [Fig. 3(c)]. For the real potential ($\kappa_+ = \kappa_-$), the input energy in the zeroth-order diffraction mode flows into the higher-order diffraction modes with both positive and negative diffraction orders; in this situation, the intensities of the first- and second-order diffraction modes (i.e., $|S_1|^2$ and $|S_2|^2$) are the same with those of the negative first- and negative second-order diffraction modes (i.e., $|S_{-1}|^2$ and $|S_{-2}|^2$), respectively, emerging a symmetric Bragg diffraction. For the complex potential ($\kappa_+ = 1.5\kappa_-$), on the other hand, the input energy in the zeroth-order diffraction mode flows mainly into the higher-order diffraction modes with negative orders; in this case, $|S_1|^2$ and $|S_2|^2$ are much smaller than $|S_{-1}|^2$ and $|S_{-2}|^2$, respectively, emerging as an asymmetric Bragg diffraction. Figure 3(b) [3(d)] shows the same as that of Fig. 3(a) [3(c)] but as a function of the diffraction angle $\theta^m_{\rm diff}$ and $\zeta = z/L_{\rm EIG}$. From this figure, we clearly see that real EIG potential [for $\kappa_+ = \kappa_-$; panels (a) and (b)] results in the formation of a symmetric Bragg diffraction, but complex EIG potential [for $\kappa_+ = 1.5\kappa_-$; panels (c) and (d)] results in the formation of an asymmetric Bragg diffraction.

The degree of asymmetry of the diffraction intensity distribution can be described by the symmetry degree $D_{\rm sym}$, with

$$D_{\rm sym}(\zeta) \equiv \frac{|S_1(\zeta)|^2}{|S_{-1}(\zeta)|^2}, \quad (22)$$

i.e., the ratio between the intensities of the first-order diffraction mode and that of the negative first-order one. The

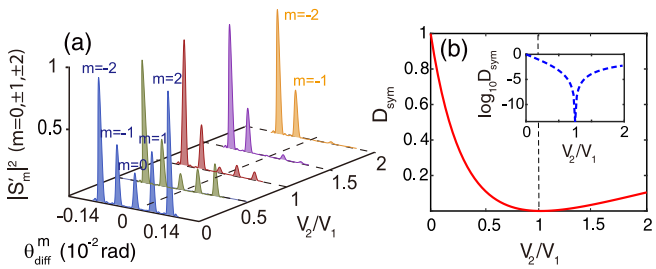

FIG. 4. Intensity distribution of linear Bragg diffraction modes and its manipulation by the $\mathcal{PT}$ symmetry of the electromagnetically induced grating (EIG). (a) Normalized mode intensities $|S'_m(\zeta)|^2$ ($m = 0, \pm1, \pm2$; each mode intensity is normalized by its maximum) as functions of the diffraction angle $\theta^m_{\rm diff}$ and the ratio between the imaginary and real parts of the EIG potential V, i.e., V_2/V_1, at $z = L_{\rm EIG}$. The mode index m is indicated for the mode intensities at $V_2/V_1 = 0$ and 2. (b) Symmetry degree of the diffraction pattern $D_{\rm sym}$ as a function of V_2/V_1. Inset: $\log_{10} D_{\rm sym}$ as a function of V_2/V_1. The minimum of $D_{\rm sym}$ arrives at the $\mathcal{PT}$ symmetry-breaking point $V_2/V_1 = 1$.

diffraction is symmetric when $D_{\rm sym} = 1$; while it becomes asymmetric if $D_{\rm sym} \neq 1$. We find that the symmetry degree $D_{\rm sym}(\zeta)$ depends significantly on the ratio between the imaginary and real parts of the EIG potential, i.e., V_2/V_1.

Plotted in Fig. 4(a) is the diffraction intensity distribution as a function of the diffraction angle $\theta^m_{\rm diff}$ and the ratio between the imaginary and real parts of the EIG potential, i.e., V_2/V_1, at $z = L_{\rm EIG}$. It is obvious that the diffraction pattern becomes more and more biased as V_2/V_1 increases from 0 to 1. Figure 4(b) shows the symmetry degree $D_{\rm sym}$ as a function of V_2/V_1. It is seen that $D_{\rm sym}$ decreases rapidly from 1 to nearly 0 as V_2/V_1 increases from 0 to 1 and then increases slowly as V_2/V_1 proceeds to increase from 1 to 2. In the inset, we show $\log_{10} D_{\rm sym}$ as a function of V_2/V_1. The minimum of $D_{\rm sym}$ is almost zero (of the order of 10^{-13}), arriving at $V_2/V_1 = 1$ (i.e., the $\mathcal{PT}$ symmetry-breaking point). Thus, the Bragg diffraction pattern becomes the most asymmetric when the $\mathcal{PT}$-symmetric EIG potential works on the symmetry-breaking point.

To understand the above result, we notice that the EIG potential can be rewritten as

$$V(\xi) = V_0 - \frac{V_1 - V_2}{2} e^{iK\xi} - \frac{V_1 + V_2}{2} e^{-iK\xi}, \tag{23}$$

which has two components $e^{iK\xi}$ and $e^{-iK\xi}$, representing two moving lattices toward the positive and negative x directions. When $V_2 = 0$, the moving lattices toward the positive and negative directions have the same amplitudes, resulting in a symmetric diffraction [Fig. 3(a)]. However, when $V_2 \neq 0$, the moving lattices toward the positive and negative directions have different amplitudes, resulting in an asymmetric diffraction [Fig. 3(c)]. When $V_1 = V_2$, i.e., at the $\mathcal{PT}$ symmetry-breaking point, there is only one lattice moving toward the negative direction $e^{-iK\xi}$, and hence, the most asymmetric diffraction pattern emerges.

Indeed, when $V_1 = V_2$, one has $\kappa_- = 0$. Thereby, Eq. (18) is reduced to

$$\frac{dS_m(\zeta)}{d\zeta} = i[-\lambda m^2 K^2 S_m(\zeta) + \kappa_+ S_{m-1}(\zeta)], \tag{24}$$

which means there is no energy transport from the mode S_m to the mode S_{m+1}, i.e., the flow of energy between adjacent diffraction modes is *unidirectional*.

IV. NONLINEAR BRAGG DIFFRACTIONS BY $\mathcal{PT}$-SYMMETRIC EIGs

We now turn to consider the nonlinear Bragg diffraction by the EIG potential. This occurs if the input probe beam becomes stronger (i.e., $|U(\xi, \zeta)| \geqslant 1$), so that the nonlinear effect in the system may bring a significant influence on the Bragg diffraction. In this case, the Kerr nonlinear term in Eq. (4) cannot be neglected. To consider the Kerr nonlinearity and give a systematic analysis on the nonlinear Bragg diffraction, we employ the method of multiple scales [86,87] to solve Eq. (4) based on the asymptotic expansion $U = \epsilon^{3/2}[U^{(1)} + \epsilon U^{(2)} + \epsilon^2 U^{(3)} + \cdots]$ (with ϵ the small parameter defined in the last section) and introduce the multiscale variables $\xi_j = \epsilon^j \xi$ ($j = 0, 1$) and $\zeta_l = \epsilon^l \zeta$ ($l = 0, 1, 2$). By substituting the expansion into Eq. (4) and using the chain rule for differentiation in the equation, we obtain the leading-order equation [like Eq. (18)] at $\epsilon^{3/2}$ order, which admits the solution:

$$U^{(1)} = q(\xi_1, \zeta_1, \zeta_2) S_m(\zeta_0) \exp(imK\xi_0). \tag{25}$$

Here, $q(\xi_1, \zeta_1, \zeta_2)$ is a slowly varying function of whole diffraction modes due to the effect of the Kerr nonlinearity.

At $\epsilon^{5/2}$ order, we get the linear equation for the function q, which is given by $i(\partial q/\partial \zeta_1) = 0$. Thus, q is independent on the variable ζ_1. To include the Kerr effect, we need to consider the higher-order of expansion. At $\epsilon^{7/2}$ order, we get the nonlinear equation of q, which is given by

$$i\frac{\partial q}{\partial \zeta} + \lambda \frac{\partial^2 q}{\partial \xi^2} + \int d\xi' W(\xi' - \xi) |q(\xi', \zeta)|^2 q(\xi, \zeta) = 0, \tag{26}$$

in terms of original coordinate variables. Note that the Bragg diffraction pattern in the nonlinear regime depends not only on the intensity of each diffraction mode $|S_m(\zeta_0)|^2$ but also on the intensity of the whole diffraction pattern $|q(\xi, \zeta)|^2$.

For extracting more information of the function q, we need to solve Eq. (26), which is nonintegrable and usually can be treated only by resorting to numerical methods. However, when the system is in the *weak* or *strong* nonlocality regimes, one can still find analytical solutions. In the weak nonlocality regime, the width of the nonlocal response function $W(\xi' - \xi)$ is finite but much narrower than that of $|q(\xi', \zeta)|^2$. Consequently, one can expand $|q(\xi', \zeta)|^2$ around $\xi' = \xi$, and Eq. (26) is reduced to the form [88]:

$$i\frac{\partial q}{\partial \zeta} + \lambda \frac{\partial^2 q}{\partial \xi^2} + \left(|q|^2 + R\frac{\partial^2 |q|^2}{\partial \xi^2}\right) q = 0, \tag{27}$$

where $R = \frac{1}{2}\int \xi^2 W(\xi) d\xi$ is a parameter characterized the weak nonlocality of the Kerr nonlinearity.

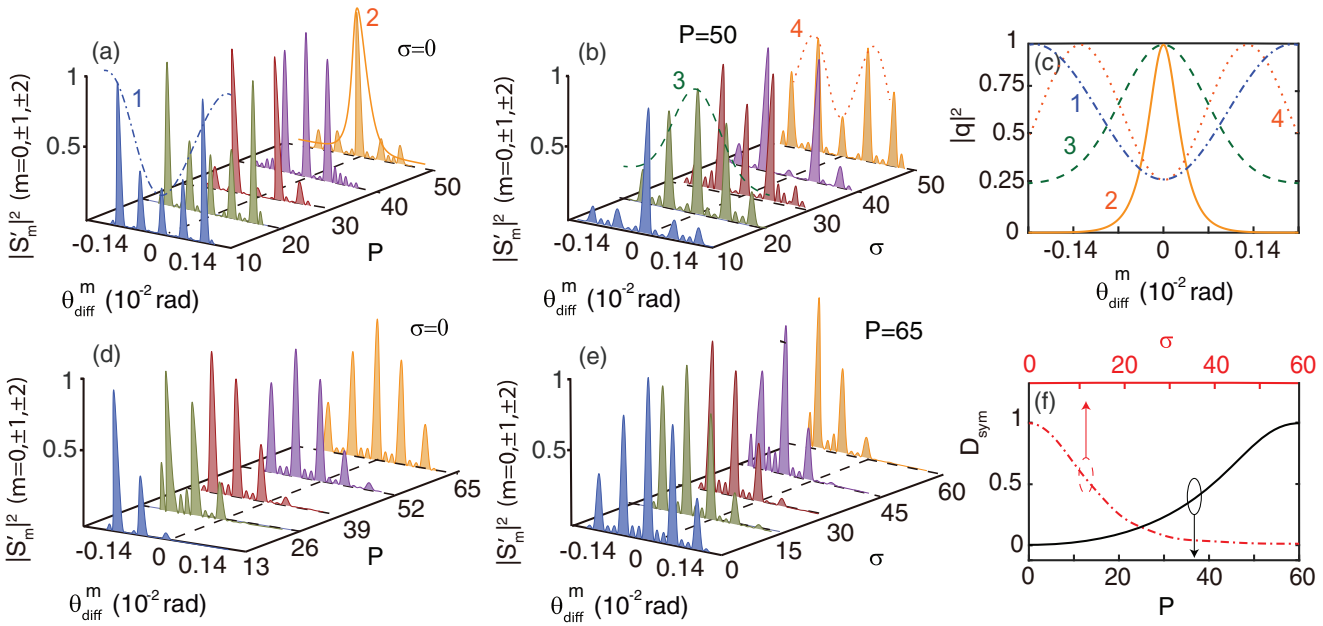

FIG. 5. Nonlinear Bragg diffraction and its control by tuning the incident light power P and nonlocality of the Kerr nonlinearity σ. (a) Normalized mode intensities $|S'_m|^2$ ($m = 0, \pm1, \pm2$; each mode intensity is normalized by its maximum) at $z = L_{\rm EIG}$ for a real electromagnetically induced grating (EIG) potential, by taking them as functions of the diffraction angle $\theta^m_{\rm diff}$ and P for $\sigma = 0$. (b) The same as (a) but by taking $|S'_m|^2$ as functions of $\theta^m_{\rm diff}$ and σ for $P = 50$. (c) Diffraction pattern intensity $|q|^2$ as a function of $\theta^m_{\rm diff}$ for $(P, \sigma) = (10, 0)$ (blue dash-dotted line; line 1), $(P, \sigma) = (50, 0)$ (yellow solid line; line 2), $(50, 20)$ (green dashed line; line 3), and $(50, 50)$ (yellow dotted line; line 4). (d) and (e) The same as (a) and (b), respectively, but for a complex $\mathcal{PT}$-symmetric EIG potential at $V_2/V_1 = 1$, i.e., at the $\mathcal{PT}$ symmetry-breaking point. (f) Symmetry degree $D_{\rm sym}$ as a function of P (black solid line) and σ (red dash-dotted line).

Equation (27) can be solved analytically and allows bright soliton solutions. Assuming $q(\xi, \zeta) = \varphi(\xi)e^{i\phi\zeta}$, we obtain that the amplitude $\varphi(\xi)$ satisfies the equation [89]:

$$\pm\sqrt{\frac{1}{2\lambda}}\,\xi = \left(\frac{1}{\varphi_0}\right)\tanh^{-1}\left(\frac{\rho}{\varphi_0}\right) + \sqrt{\frac{2R}{\lambda}}\,\tanh^{-1}\left(\sqrt{\frac{2R}{\lambda}}\,\rho\right), \tag{28}$$

where $\rho^2 = (\varphi_0^2 - \varphi^2)/(1 + 2R\varphi^2/\lambda)$, the peak amplitude $\varphi_0 = \varphi(\xi = 0)$, and the phase $\phi = \varphi_0^2/2$. At the local limit, $W(\xi) \to \delta(\xi)$, and hence $R \to 0$, we recover from Eq. (28) the well-known hyperbolic secant profile $\varphi(\xi) = \varphi_0\,\mathrm{sech}(\varphi_0\xi)$.

In the strong nonlocality regime, the width of the response function $W(\xi' - \xi)$ is much wider than $|q(\xi', \zeta)|^2$. Consequently, one can expand $W(\xi' - \xi)$ around $\xi' = \xi$, and hence, Eq. (26) is reduced to the form [88]:

$$i\frac{\partial q}{\partial \zeta} + \lambda\frac{\partial^2 q}{\partial \xi^2} + \left(Q_0 - Q_2\xi^2\right)q = 0, \tag{29}$$

where the coefficients:

$$Q_0 = \mathrm{Re}(W)|_{\xi=0}Q, \qquad Q_2 = -\frac{1}{2}\frac{d^2\mathrm{Re}(W)}{d\xi^2}\bigg|_{\xi=0}Q,$$

with the constant $Q = \int |q|^2 d\xi$. Since $Q_{0,2} > 0$ [see Fig. 1(c)], Eq. (29) has the form of the Schrödinger equation for a linear harmonic oscillator, whose solution can be written as $q(\xi, \zeta) = \varphi(\xi)e^{i\phi\zeta}$, with the amplitude:

$$\varphi(\xi) = \frac{1}{\sqrt{\sqrt{2\pi}2^n n!}}H_n\left(\sqrt[4]{\frac{Q_2}{\lambda}}\,\xi\right)\exp\left(-\sqrt{\frac{Q_2}{\lambda}}\,\frac{\xi^2}{2}\right), \tag{30}$$

and the phase $\phi = Q_0 - \sqrt{\lambda Q_2}(2n + 1)$. Here, $H_n(\cdot)$ is the nth Hermite polynomial. When $n = 0$, the amplitude (phase) is reduced to the form $\varphi(\xi) = (1/\sqrt[4]{2\pi})\exp(-\sqrt{Q_2/\lambda}\,\xi^2/2)$ ($\phi = Q_0 - \sqrt{\lambda Q_2}$). At the limit of strong nonlocality, $W(\xi) \to W(\xi = 0)$, and hence $Q_2 \to 0$, the solution becomes $\varphi(\xi) = \varphi_0\cos(\sqrt{(Q_0 - \phi)/\lambda}\,\xi)$, which is not a localized solution in the x direction any more.

The above analytical results are confirmed by carrying out numerical simulation. Figures 5(a), 5(b), 5(d), and 5(e) show the spatial distribution of nonlinear Bragg diffraction and its control through tuning the incident light power $P \equiv \int_{-\infty}^{\infty} d\xi |U(\xi, \zeta = 0)|^2$ and nonlocality of the Kerr nonlinearity. The nonlocal property of the Kerr nonlinearity can be characterized by the nonlocality degree, defined as

$$\sigma = \frac{R_b}{w_0}. \tag{31}$$

The weakly nonlocal Kerr nonlinearity has a small value of σ, whereas the strongly nonlocal Kerr nonlinearity has a large value of σ.

Plotted in Fig. 5(a) is the diffraction intensity distribution $|S_m|^2$ ($m = 0, \pm1, \pm2$) at $z = L_{\rm EIG}$ for a real EIG potential ($V_1 = 0.01, V_2 = 0$) in the plane of the diffraction angle $\theta^m_{\rm diff}$ and the incident light power P at the local limit of Kerr nonlinearity ($\sigma = 0$). From the figure, we see that, at the local limit, the energy of the light field becomes more and more

focused in the zeroth-order diffraction mode as P grows (which can be clearly seen when P is increased to 50, illustrated by the yellow peaks in this figure). The physical reason for this increased self-focusing of the diffraction pattern is due to the growth of the Kerr nonlinearity when P increases. The blue dash-dotted line (line 1) and the yellow solid line (line 2) correspond to the function $|q|^2$ for $(P,\sigma)=(10,0)$ and $(P,\sigma)=(50,0)$, respectively.

Plotted in Fig. 5(b) is the diffraction intensity distribution $|S_m|^2$ $(m=0,\pm1,\pm2)$ at $z=L_{\rm EIG}$ as a function of $\theta_{\rm diff}^m$ and σ for a strong incident light power $P=50$. We see that, when σ is increased, the light energy is likely to distribute uniformly among all diffraction orders, and hence, the diffraction pattern becomes more extended (which can be clearly seen when σ is increased to 50, illustrated by the yellow peaks in this figure). The spreading of the diffraction pattern in this case is attributed to the increase of the nonlocality of the Kerr nonlinearity, which plays an opposite role against the magnitude of the focusing Kerr nonlinearity. The green dashed line (line 3) and yellow dotted line (line 4) correspond to the function $|q|^2$ for $(P,\sigma)=(50,20)$ and $(50,50)$, respectively.

To illustrate the Kerr nonlinear effect on the Bragg diffraction more clearly, in Fig. 5(c), we show $|q|^2$ as a function of $\theta_{\rm diff}^m$ for $(P,\sigma)=(10,0)$, $(50,0)$, $(50,20)$, and $(50,50)$, given respectively by the blue dash-dotted line (line 1), yellow solid line (line 2), green dashed line (line 3), and yellow dotted line (line 4). These lines correspond to the linear Bragg diffraction at the local limit (line 1), the nonlinear Bragg diffraction at the local limit (line 2), the nonlinear Bragg diffraction in the strongly nonlocal regime (line 3), and the nonlinear Bragg diffraction at the nonlocal limit (line 4). From the figure, we see that the diffraction pattern given by lines 1 and 4 are extended, which is due to the absence of Kerr nonlinearity (line 1) and strong nonlocality (line 4). The diffraction pattern given by line 2 is rather localized (like a hyperbolic secant soliton) due to the strong Kerr nonlinearity at the local limit. The diffraction pattern given by line 3 is also localized; however, it is less localized than that given by line 2 because of the increased nonlocality of the Kerr nonlinearity.

The behavior of the nonlinear Brag diffraction by a complex $\mathcal{PT}$-symmetric EIG potential is displayed in Figs. 5(d) and 5(e), corresponding to Figs. 5(a) and 5(b), respectively. Since the complex $\mathcal{PT}$-symmetric EIG potential works at $V_2/V_1=1$ (i.e., at the $\mathcal{PT}$ symmetry-breaking point), the diffraction pattern for $(P,\sigma)=(13,0)$, corresponding to the linear Bragg diffraction at the local limit, is strongly asymmetric. However, the asymmetric diffraction pattern restores its symmetry when P is increased at the local limit $(\sigma=0)$ [Fig. 5(d)] and loses its symmetry by increasing the nonlocality of the Kerr nonlinearity when P is fixed $(P=65)$ [Fig. 5(e)]. Shown in Fig. 5(f) is the symmetry degree of the diffraction patterns $D_{\rm sym}$ as a function of the incident light power P (the nonlocality degree σ). It is seen that $D_{\rm sym}$ is increased when P increases. It is decreased, however, when σ increases.

The generation power of the nonlinear Bragg diffraction shown in Fig. 5 can be estimated by computing the corresponding Poynting's vector integrated over the cross-sectional area of the probe beam, which is given by

$$P_{\rm gen}=2\varepsilon_0 c n_p S_0\left(\frac{2\hbar}{p_{13}}\right)^2|\Omega_p|^2\approx 1.8\,{\rm nW}, \tag{32}$$

where S_0 is the cross-sectional area of the probe beam ($S_0\sim 10^4\ \mu{\rm m}^2$). From the value of $P_{\rm gen}$, we find that, in the present system, a very low input power is sufficient for creating the nonlinear Bragg diffraction, which is due to the presence of giant nonlocal Kerr nonlinearity contributed by strong Rydberg-Rydberg interaction between atoms. This fact may be highly beneficial for the exploration of nonlinear Bragg diffraction in the regime of quantum optics, as well as facilitate more applications in the fields of optical information processing and transmission.

V. BRAGG DIFFRACTION MANIPULATED BY A GRADIENT MAGNETIC FIELD

Light fields interacting with multilevel atoms can be controlled by using gradient magnetic fields [90,91]. Such a technique can also be used to manipulate the Bragg diffraction of the probe beam by the $\mathcal{PT}$-symmetric EIG in the present system. For this aim, we consider that a weak gradient magnetic field:

$$\mathbf{B}(x)=\hat{\mathbf{z}}B(x)=\hat{\mathbf{z}}B_0 x, \tag{33}$$

is applied to the system, where $\hat{\mathbf{z}}$ is the unit vector in the z direction, and B_0 characterizes the gradient of the magnetic field in the x direction. Due to the presence of the magnetic field, each level of the atoms is split into a series of Zeeman sublevels with energy $\Delta E_{\alpha,\rm Zeeman}=\mu_{\rm B}g_F^\alpha m_F^\alpha B$, where $\mu_{\rm B}$, g_F^α, and m_F^α are the Bohr magneton, gyromagnetic factor, and magnetic quantum number of level $|\alpha\rangle$, respectively. As a result, the one- and two-photon detunings are modified as $\tilde{\Delta}_2=\Delta_2+\mu_{21}B_0x$, $\tilde{\Delta}_3=\Delta_3+\mu_{31}B_0x$, and $\tilde{\Delta}_4=\Delta_4+\mu_{41}B_0x$, with $\mu_{\alpha\beta}=\mu_{\rm B}(g_F^\alpha m_F^\alpha-g_F^\beta m_F^\beta)/\hbar$. For the strontium atoms and the given parameters, we have $\mu_{21}=6\times10^9$ C kg^{-1}, $\mu_{31}=4.6\times10^9$ C kg^{-1}, and $\mu_{41}=3\times10^9$ C kg^{-1}.

The Zeeman shift of atomic levels is equivalent to an external force acting on the atoms, which acts back to the probe field in the system. As a result, an external potential related to the magnetic field will appear in the envelope equation of the probe field. By employing a similar derivation as that given in Sec. II A, we get the nonlinear envelope equation for the probe beam:

$$\begin{aligned} i\frac{\partial q}{\partial\zeta}+\lambda\frac{\partial^2 q}{\partial\xi^2}+\int d\xi' W(\xi'-\xi)|q(\xi',\zeta)|^2 q(\xi,\zeta)\\ +V_m(B_0)\xi q\\ =0, \end{aligned} \tag{34}$$

where the magnetic-field-induced potential is given by $V_m(B_0)=L_{\rm EIG}w_0\kappa_{13}(M_{21}\mu_{21}+M_{31}\mu_{31}+M_{41}\mu_{41})B_0$, with

$$M_{21}=\frac{d_{41}\left[\rho_{33}^{(0)}-\rho_{11}^{(0)}\right]-\Omega_a^*\rho_{43}^{(0)}}{D}+\alpha_{31}^{(1)}\frac{d_{31}d_{41}-|\Omega_a|^2}{|D|^2},$$

$$M_{31}=\alpha_{31}^{(1)}\frac{d_{21}d_{41}}{|D|^2},$$

$$M_{41}=\frac{d_{21}\left[\rho_{33}^{(0)}-\rho_{11}^{(0)}\right]-\Omega_c\rho_{23}^{(0)}}{D}+\alpha_{31}^{(1)}\frac{d_{21}d_{31}-|\Omega_c|^2}{|D|^2},$$

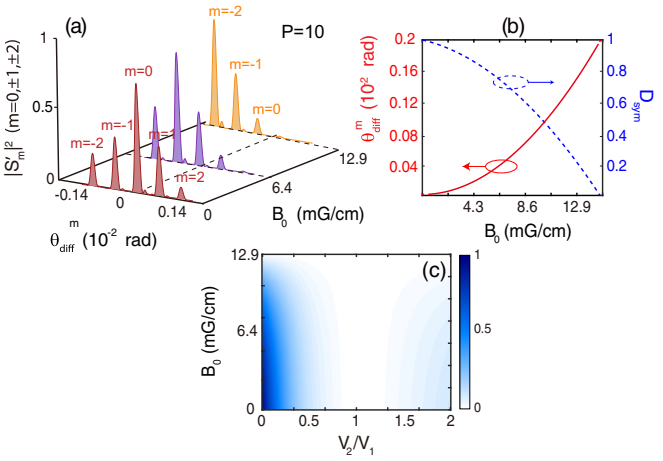

FIG. 6. Nonlinear Bragg diffraction manipulated by an applied gradient magnetic field. (a) Normalized mode intensities $|S'_m|^2$ ($m = 0, \pm1, \pm2$; each mode intensity is normalized by its maximum) as functions of the diffraction angle $\theta^m_{\rm diff}$ and the magnetic-field gradient B_0 with the incident light power $P = 10$ at $z = L_{\rm EIG}$. (b) Diffraction angle $\theta^m_{\rm diff}$ of the largest diffraction mode (red solid line) and symmetry degree $D_{\rm sym}$ (blue dashed line) as functions of B_0. (c) Symmetry degree $D_{\rm sym}$ as a function of V_2/V_1 and B_0. The blue (white) region corresponds to the emergence of symmetric (asymmetric) diffraction pattern.

and $D = d_{21}d_{31}d_{41} - |\Omega_c|^2 d_{41} - |\Omega_a|^2 d_{21}$. Here, $d_{\alpha\beta} = \Delta_\alpha - \Delta_\beta + i\gamma_{\alpha\beta}$, with $\gamma_{\alpha\beta}$ the decay rate from $|\beta\rangle$ to $|\alpha\rangle$.

For illustrating how the gradient magnetic field affects the Bragg diffraction, as a first step, we consider Eq. (34) in the absence of the nonlocal Kerr nonlinearity. By using the transformations:

$$q' = q\exp\left[-i\left(\frac{V_m\xi'}{2\lambda} + \frac{V_m^2\zeta'^2}{12\lambda^2}\right)\zeta'\right],$$
$$\xi' = \xi - \frac{V_m\zeta'^2}{(4\lambda)}, \quad \zeta' = 2\lambda\zeta, \tag{35}$$

Eq. (34) is converted into the form $i\partial q'/\partial\zeta' + (\frac{1}{2})(\partial^2 q'/\partial\xi'^2) = 0$. Assuming the input probe beam is a wave packet, it is easy to obtain the expression of the trajectory of the central position of the probe beam, i.e., $\xi = V_m\lambda\zeta^2$, which turning back to the original variables reads

$$x = \frac{w_0^2}{L_{\rm diff}}\kappa_{13}(M_{21}\mu_{21} + M_{31}\mu_{31} + M_{41}\mu_{41})B_0 z^2. \tag{36}$$

We see that, due to the presence of the magnetic field, the trajectory of the central position in the x direction has a deflection with a quadratic dependence on the propagation coordinate z; moreover, the trajectory can be controlled by tuning the gradient of the magnetic field, i.e., by the control parameter B_0.

In the presence of the nonlocal Kerr nonlinearity, it is not easy to get an exact expression for the trajectory of the central position of the probe beam. In this case, we resort to a numerical simulation for solving Eq. (34) directly. Shown in Fig. 6(a) is the diffraction pattern as a function of the diffraction angle $\theta^m_{\rm diff}$ and the magnetic gradient B_0 with the incident light power $P = 10$ (corresponding to a weak input probe beam) at $z = L_{\rm EIG}$. One sees that the diffraction pattern becomes more and more biased when B_0 increases. Figure 6(b) shows the diffraction angle $\theta^m_{\rm diff}$ of the largest diffraction mode and the symmetry degree $D_{\rm sym}$ as functions of B_0. It is seen that $\theta^m_{\rm diff}$ is increased when B_0 increases, whereas $D_{\rm sym}$ is decreased as B_0 increases.

Finally, in Fig. 6(c), we plotted the result of the symmetry degree $D_{\rm sym}$ of the Bragg diffraction pattern as a function of the ratio between the imaginary and real parts of the $\mathcal{PT}$-symmetric EIG potential V (i.e., V_2/V_1) and the magnetic-field gradient B_0. As expected, for large V_2/V_1 or large B_0, $D_{\rm sym}$ has small values, which means that the diffraction pattern is highly asymmetric; particularly, when V_2/V_1 is close to one or B_0 is very large, $D_{\rm sym}$ is nearly vanishing. Therefore, the diffraction pattern of the probe beam can be controlled not only by the $\mathcal{PT}$-symmetry property of the EIG through the ratio V_2/V_1 but also by the gradient magnetic field through the gradient B_0.

VI. SUMMARY

In summary, we have proposed a scheme for realizing a tunable EIG with $\mathcal{PT}$ symmetry in a cold gas of Rydberg atoms and investigated linear and nonlinear Bragg diffractions and their active control. We have shown that a laser beam with very low light intensity incident upon the $\mathcal{PT}$-symmetric EIG can display distinctive nonlinear diffraction patterns, which can be actively manipulated through tuning the gain-absorption coefficient of the EIG and the input power of the laser beam. We have also shown that the patterns of intensity distribution among different diffraction modes depend significantly on the $\mathcal{PT}$-symmetry property of the EIG and on the magnitude and nonlocality degree of the Kerr nonlinearity. In addition, an external gradient magnetic field can be used to provide a different way for manipulating the nonlinear Bragg diffraction. The results reported here are not only beneficial for understanding the unique properties of nonlinear Bragg diffraction by $\mathcal{PT}$-symmetric EIGs but also useful for designing optical devices applicable in the areas of optical information processing and transmission.

ACKNOWLEDGMENTS

This paper was supported by the National Natural Science Foundation of China under Grants No. 11974117 and No. 11975098, National Key Research and Development Program of China under Grant No. 2017YFA0304201, and Shanghai Municipal Science and Technology Major Project under Grant No. 2019SHZDZX01.

APPENDIX: BLOCH EQUATIONS AND SOLUTIONS OF DM ELEMENTS AT DIFFERENT ORDERS

1. Bloch equations

The optical Bloch equations for single atomic DM elements $\rho_{\alpha\beta} \equiv \langle \hat{S}_{\alpha\beta} \rangle$ ($\alpha, \beta = 1, 2, 3, 4$) read [84]

$$i\frac{\partial}{\partial t}\rho_{11} + i\Gamma_{21}\rho_{11} - i\Gamma_{13}\rho_{33} - \Omega_p\rho_{13} + \Omega_p^*\rho_{31} = 0, \tag{A1a}$$

$$i\frac{\partial}{\partial t}\rho_{22} - i\Gamma_{21}\rho_{11} - i\Gamma_{23}\rho_{33} - \Omega_c\rho_{23} + \Omega_c^*\rho_{32} = 0, \tag{A1b}$$

$$i\frac{\partial}{\partial t}\rho_{33} + i\Gamma_3\rho_{33} - i\Gamma_{34}\rho_{44} + \Omega_p\rho_{13} - \Omega_p^*\rho_{31} + \Omega_c\rho_{23} - \Omega_c^*\rho_{32} - \Omega_a\rho_{34} + \Omega_a^*\rho_{43} = 0, \tag{A1c}$$

$$i\frac{\partial}{\partial t}\rho_{44} + i\Gamma_{34}\rho_{44} + \Omega_a\rho_{34} - \Omega_a^*\rho_{43} = 0, \tag{A1d}$$

for diagonal DMs, and

$$\left(i\frac{\partial}{\partial t} + d_{21}\right)\rho_{21} + \Omega_c^*\rho_{31} - \Omega_p\rho_{23} = 0, \tag{A2a}$$

$$\left(i\frac{\partial}{\partial t} + d_{31}\right)\rho_{31} + \Omega_p(\rho_{11} - \rho_{33}) + \Omega_c\rho_{21} + \Omega_a^*\rho_{41} = 0, \tag{A2b}$$

$$\left(i\frac{\partial}{\partial t} + d_{41}\right)\rho_{41} + \Omega_a\rho_{31} - \Omega_p\rho_{43} - N_a\int d^3r' V(r'-r)\rho_{44,41}(r', r, t) = 0, \tag{A2c}$$

$$\left(i\frac{\partial}{\partial t} + d_{32}\right)\rho_{32} + \Omega_c(\rho_{22} - \rho_{33}) + \Omega_p\rho_{12} + \Omega_a^*\rho_{42} = 0, \tag{A2d}$$

$$\left(i\frac{\partial}{\partial t} + d_{42}\right)\rho_{42} + \Omega_a\rho_{32} - \Omega_c\rho_{43} - N_a\int d^3r' V(r'-r)\rho_{44,42}(r', r, t) = 0, \tag{A2e}$$

$$\left(i\frac{\partial}{\partial t} + d_{43}\right)\rho_{43} + \Omega_a(\rho_{33} - \rho_{44}) - \Omega_p^*\rho_{41} - \Omega_c^*\rho_{42} - N_a\int d^3r' V(r'-r)\rho_{44,43}(r', r, t) = 0, \tag{A2f}$$

for off-diagonal DMs. Here, $d_{\alpha\beta} = \Delta_\alpha - \Delta_\beta + i\gamma_{\alpha\beta}$, with $\gamma_{\alpha\beta} = (\Gamma_\alpha + \Gamma_\beta)/2 + \gamma_{\alpha\beta}^{\rm dep}$. Here, $\Gamma_\beta = \sum_{\alpha<\beta}\Gamma_{\alpha\beta}$, with $\Gamma_{\alpha\beta}$ the spontaneous emission decay rate and $\gamma_{\alpha\beta}^{\rm dep}$ the dephasing rate from $|\beta\rangle$ to $|\alpha\rangle$. Note that we have used the notation $\rho_{\alpha\beta,\mu\nu}(r', r, t) \equiv \langle \hat{S}_{\alpha\beta}(r', t)\hat{S}_{\mu\nu}(r', t)\rangle$, which are two-atom DMs coming from the Rydberg-Rydberg interaction in the system.

2. Solutions of DM elements at different orders

The solution of the optical Bloch equations given above can be solved by taking a perturbation expansion $\rho_{\alpha\beta} = \rho_{\alpha\beta}^{(0)} + \epsilon\rho_{\alpha\beta}^{(1)} + \epsilon^2\rho_{\alpha\beta}^{(2)} + \epsilon^3\rho_{\alpha\beta}^{(3)} + \cdots$ and assuming Ω_p/Ω_c as a small parameter. Since the two-photon detuning Δ_4 is large, we can assume that the atomic population in the Rydberg state $|4\rangle$ is approximated to zero, i.e., $\rho_4^{(0)} = 0$. Thus, at the zeroth order of perturbation expansion, we obtain equations for $\rho_{11}^{(0)}$, $\rho_{22}^{(0)}$, and $\rho_{33}^{(0)}$, given by

$$\begin{pmatrix} -\Gamma_{21} & 0 & \Gamma_{13} \\ \Gamma_{21} & 0 & \Gamma_{23} \\ 1 & 1 & 1 \end{pmatrix}\begin{bmatrix} \rho_{11}^{(0)} \\ \rho_{22}^{(0)} \\ \rho_{33}^{(0)} \end{bmatrix} = \begin{Bmatrix} 0 \\ 2\,\mathrm{Im}\left[\Omega_c^*\rho_{32}^{(0)}\right] \\ 1 \end{Bmatrix}. \tag{A3}$$

To solve $\rho_{32}^{(0)}$, we also need equations for $\rho_{32}^{(0)}$, $\rho_{42}^{(0)}$, and $\rho_{43}^{(0)}$, which are given by

$$\begin{pmatrix} d_{32} & \Omega_a^* & 0 \\ \Omega_a & d_{42} & -\Omega_c \\ 0 & -\Omega_c^* & d_{43} \end{pmatrix}\begin{bmatrix} \rho_{32}^{(0)} \\ \rho_{42}^{(0)} \\ \rho_{43}^{(0)} \end{bmatrix} = \begin{Bmatrix} \Omega_c\left[\rho_{33}^{(0)} - \rho_{22}^{(0)}\right] \\ 0 \\ -\Omega_a\rho_{33}^{(0)} \end{Bmatrix}. \tag{A4}$$

The solutions of Eqs. (A3) and (A4) are given as

$$\rho_{11}^{(0)} = -\frac{\Gamma_{13}X}{\Gamma_{21}\Gamma_{13} - (\Gamma_{21} + \Gamma_{13})X + \Gamma_{21}(\Gamma_{23} + Y)}, \tag{A5}$$

$$\rho_{22}^{(0)} = \frac{\Gamma_{21}(\Gamma_{13} + \Gamma_{23} + Y)}{\Gamma_{21}\Gamma_{13} - (\Gamma_{21} + \Gamma_{13})X + \Gamma_{21}(\Gamma_{23} + Y)}, \tag{A6}$$

$$\rho_{33}^{(0)} = -\frac{\Gamma_{21}X}{\Gamma_{21}\Gamma_{13} - (\Gamma_{21} + \Gamma_{13})X + \Gamma_{21}(\Gamma_{23} + Y)}, \tag{A7}$$

$$\rho_{32}^{(0)} = \frac{\left[-(d_{42}d_{43} - |\Omega_c|^2)\rho_{22}^{(0)} + (d_{42}d_{43} - |\Omega_c|^2 + |\Omega_a|^2)\rho_{33}^{(0)}\right]\Omega_c}{Z}, \tag{A8}$$

$$\rho_{42}^{(0)} = \frac{\left[d_{43}\rho_{22}^{(0)} - (d_{32} + d_{43})\rho_{33}^{(0)}\right]\Omega_c\Omega_a}{Z}, \tag{A9}$$

$$\rho_{43}^{(0)} = \frac{\left[|\Omega_c|^2\rho_{22}^{(0)} - (d_{32}d_{42} + |\Omega_c|^2 - |\Omega_a|^2)\rho_{33}^{(0)}\right]\Omega_a}{Z}, \tag{A10}$$

with the other DM elements being zeros $[\rho_{21}^{(0)} = \rho_{31}^{(0)} = \rho_{41}^{(0)} = \rho_{44}^{(0)} = 0]$. Here, $X = 2\,\mathrm{Im}[(d_{42}d_{43} - |\Omega_c|^2)|\Omega_c|^2/Z]$ and $Y = -2\,\mathrm{Im}[(d_{42}d_{43} - |\Omega_c|^2 + |\Omega_a|^2)|\Omega_c|^2/Z]$, with $Z = d_{32}d_{42}d_{43} - |\Omega_c|^2 d_{32} - |\Omega_a|^2 d_{43}$.

At first order, the solutions for nonzero matrix elements read $\rho_{21}^{(1)} = \alpha_{21}^{(1)}\Omega_p$, $\rho_{31}^{(1)} = \alpha_{31}^{(1)}\Omega_p$, and $\rho_{41}^{(1)} = \alpha_{41}^{(1)}\Omega_p$, where $\alpha_{21}^{(1)}$, $\alpha_{31}^{(1)}$, and $\alpha_{41}^{(1)}$ are determined by the equation:

$$\begin{pmatrix} d_{21} & \Omega_c^* & 0 \\ \Omega_c & d_{31} & \Omega_a^* \\ 0 & \Omega_a & d_{41} \end{pmatrix} \begin{bmatrix} \alpha_{21}^{(1)} \\ \alpha_{31}^{(1)} \\ \alpha_{41}^{(1)} \end{bmatrix} = \begin{bmatrix} \rho_{23}^{(0)} \\ \rho_{33}^{(0)} - \rho_{11}^{(0)} \\ \rho_{43}^{(0)} \end{bmatrix}, \tag{A11}$$

leading to the solutions of $\alpha_{21}^{(1)}$, $\alpha_{31}^{(1)}$, and $\alpha_{41}^{(1)}$:

$$\begin{aligned}
\alpha_{21}^{(1)} &= \left\{(d_{31}d_{41} - |\Omega_a|^2)\rho_{23}^{(0)} + \Omega_c^*\Omega_a^*\rho_{43}^{(0)} - d_{41}\Omega_c^*\left[\rho_{33}^{(0)} - \rho_{11}^{(0)}\right]\right\}/D, \\
\alpha_{31}^{(1)} &= \left\{d_{21}d_{41}\left[\rho_{33}^{(0)} - \rho_{11}^{(0)}\right] - d_{41}\Omega_c\rho_{23}^{(0)} - d_{21}\Omega_a^*\rho_{43}^{(0)}\right\}/D, \\
\alpha_{41}^{(1)} &= \left\{(d_{21}d_{31} - |\Omega_c|^2)\rho_{43}^{(0)} + \Omega_c\Omega_a\rho_{23}^{(0)} - d_{21}\Omega_a\left[\rho_{33}^{(0)} - \rho_{11}^{(0)}\right]\right\}/D,
\end{aligned}$$

where $D = d_{21}d_{31}d_{41} - |\Omega_c|^2 d_{41} - |\Omega_a|^2 d_{21}$.

At second order, the solution for the nonzero matrix elements is found to be $\rho_{32}^{(2)} = \alpha_{32}^{(2)}|\Omega_p|^2$, $\rho_{42}^{(2)} = \alpha_{42}^{(2)}|\Omega_p|^2$, $\rho_{43}^{(2)} = \alpha_{43}^{(2)}|\Omega_p|^2$, and $\rho_{jj}^{(2)} = \alpha_{jj}^{(2)}|\Omega_p|^2$, with α_{32}, α_{42}, and α_{43} satisfying the equation:

$$\begin{pmatrix} d_{32} & \Omega_a^* & 0 \\ \Omega_a & d_{42} & -\Omega_c \\ 0 & -\Omega_c^* & d_{43} \end{pmatrix} \begin{bmatrix} \alpha_{32}^{(2)} \\ \alpha_{42}^{(2)} \\ \alpha_{43}^{(2)} \end{bmatrix} = \begin{Bmatrix} \Omega_c\left[\alpha_{33}^{(2)} - \alpha_{22}^{(2)}\right] - \alpha_{12}^{(1)} \\ 0 \\ \Omega_a\left[\alpha_{44}^{(2)} - \alpha_{33}^{(2)}\right] + \alpha_{41}^{(1)} \end{Bmatrix}, \tag{A12}$$

and $\alpha_{jj}^{(2)}$ satisfying the equation:

$$\begin{pmatrix} -\Gamma_{21} & 0 & \Gamma_{13} & 0 \\ \Gamma_{21} & 0 & \Gamma_{23} & 0 \\ 0 & 0 & -\Gamma_{13} - \Gamma_{23} & \Gamma_{34} \\ 1 & 1 & 1 & 1 \end{pmatrix} \begin{bmatrix} \alpha_{11}^{(2)} \\ \alpha_{22}^{(2)} \\ \alpha_{33}^{(2)} \\ \alpha_{44}^{(2)} \end{bmatrix} = \begin{Bmatrix} 2\,\mathrm{Im}\left[\alpha_{31}^{(1)}\right] \\ 2\,\mathrm{Im}\left[\Omega_c^*\alpha_{32}^{(2)}\right] \\ 2\,\mathrm{Im}\left[\alpha_{31}^{(1)*} + \Omega_c\alpha_{32}^{(2)*} + \Omega_a^*\alpha_{43}^{(2)}\right] \\ 0 \end{Bmatrix}. \tag{A13}$$

The nonlocal Kerr nonlinearity appears at the third order. The solution of $\rho_{jl}^{(3)}$ can be obtained from the equation:

$$\begin{pmatrix} d_{21} & \Omega_c^* & 0 \\ \Omega_c & d_{31} & \Omega_a^* \\ 0 & \Omega_a & d_{41} \end{pmatrix} \begin{bmatrix} \rho_{21}^{(3)} \\ \rho_{31}^{(3)} \\ \rho_{41}^{(3)} \end{bmatrix} = \begin{bmatrix} \alpha_{23}^{(2)} \\ \alpha_{33}^{(2)} - \alpha_{11}^{(2)} \\ \alpha_{43}^{(2)} \end{bmatrix} |\Omega_p|^2\Omega_p + \begin{bmatrix} 0 \\ 0 \\ \mathcal{N}_\alpha \int \mathbf{r}' V(\mathbf{r}' - \mathbf{r})\alpha_{4141}^{(3)}|\Omega_p(\mathbf{r}')|^2\Omega_p(\mathbf{r}) \end{bmatrix}. \tag{A14}$$

To acquire the expression of $\alpha_{4141}^{(3)}$ in the second term on the right-hand side of the above equation, we need to write the equation of the two-body DM elements from the second order, reading

$$\begin{pmatrix} d_{21} & 0 & 0 & \Omega_c^* & 0 & 0 \\ 0 & d_{31} & 0 & \Omega_c & 0 & \Omega_a^* \\ 0 & 0 & d_{41} - \frac{V}{2} & 0 & 0 & \Omega_a \\ \Omega_c & \Omega_c^* & 0 & d_{21} + d_{31} & \Omega_a^* & 0 \\ 0 & 0 & 0 & \Omega_a & d_{21} + d_{41} & \Omega_c^* \\ 0 & \Omega_a & \Omega_a^* & 0 & \Omega_c & d_{31} + d_{41} \end{pmatrix} \begin{bmatrix} \alpha_{2121}^{(2)} \\ \alpha_{3131}^{(2)} \\ \alpha_{4141}^{(2)} \\ \alpha_{2131}^{(2)} \\ \alpha_{2141}^{(2)} \\ \alpha_{3141}^{(2)} \end{bmatrix} = \begin{Bmatrix} \rho_{23}^{(0)}\alpha_{21}^{(1)} \\ \left[\rho_{33}^{(0)} - \rho_{11}^{(0)}\right]\alpha_{31}^{(1)} \\ \rho_{43}^{(0)}\alpha_{41}^{(1)} \\ \left[\rho_{33}^{(0)} - \rho_{11}^{(0)}\right]\alpha_{21}^{(1)} + \rho_{23}^{(0)}\alpha_{31}^{(1)} \\ \rho_{23}^{(0)}\alpha_{41}^{(1)} + \rho_{43}^{(0)}\alpha_{21}^{(1)} \\ \left[\rho_{33}^{(0)} - \rho_{11}^{(0)}\right]\alpha_{41}^{(1)} + \rho_{43}^{(0)}\alpha_{31}^{(1)} \end{Bmatrix}. \tag{A15}$$

After solving the above equation and obtaining the solutions of $\alpha_{j1,l1}^{(2)}$, the third-order equation of the two-body DM elements (which are too lengthy, thus not written explicitly down here) can also be solved, which have the solution of the form

$\rho^{(3)}_{jl,mn} = a^{(3)}_{jl,mn}|\Omega_p(\mathbf{r}',t)|^2\Omega_p(\mathbf{r},t)$, where $a^{(3)}_{jl,mn}$ are functions of $\mathbf{r}'-\mathbf{r}$. The solution of $\rho^{(3)}_{44,41}$ can be written as $\rho^{(3)}_{44,41}(\mathbf{r}'_1,\mathbf{r}_1) = a^{(3)}_{44,41}|F(\mathbf{r}'_1)|^2F(\mathbf{r}_1)\exp[i(Kz_0-\omega t_0)]$, with

$$a^{(3)}_{44,41} = \frac{\sum_{m=0}^{3}A_mV(\mathbf{r}'-\mathbf{r})^m}{\sum_{n=0}^{4}B_nV(\mathbf{r}'-\mathbf{r})^n}. \tag{A16}$$

Here, A_m ($m=0,1,2,3$) and B_n ($n=0,1,2,3,4$) are complex constants depending on the spontaneous emission decay rate Γ_{jl}, the dephasing rate $\gamma^{\rm dep}_{jl}$, the detuning Δ_j, and the half Rabi frequencies Ω_a and Ω_c; their explicit expressions are too lengthy, thus omitted here.

Finally, by keeping the terms up to the third order, we obtain $\rho_{31} = \rho^{(1)}_{31} + \rho^{(3)}_{31}$, reading

$$\begin{aligned}\rho_{31} = {}& \alpha^{(1)}_{31}\Omega_p + \left\{\frac{d_{21}d_{41}}{D}[\alpha^{(2)}_{33}-\alpha^{(2)}_{11}] - \frac{d_{41}\Omega_c}{D}\alpha^{(2)}_{23} - \frac{d_{21}\Omega^*_a}{D}\alpha^{(2)}_{43}\right\}|\Omega_p|^2\Omega_p \\ & - \frac{d_{21}\Omega^*_a}{D}\mathcal{N}_\alpha\int \mathbf{r}'V(\mathbf{r}'-\mathbf{r})\alpha^{(3)}_{4141}|\Omega_p(\mathbf{r}')|^2\Omega_p(\mathbf{r}),\end{aligned} \tag{A17}$$

with D being the same as that used in the solutions of $\alpha^{(1)}_{21}$, $\alpha^{(1)}_{31}$, and $\alpha^{(1)}_{41}$.

[1] M. Born and E. Wolf, *Principles of Optics*, 7th (expanded) ed. (Cambridge University Press, Cambridge, 1999).

[2] E. G. Loewen and E. Popov, *Diffraction Gratings and Applications (Optical Science and Engineering)*, 1st ed. (CRC Press Inc., Boca Raton, 1997).

[3] C. Palmer and E. G. Loewen, *Diffraction Grating Handbook* (Newport Corp., Rochester, 2005).

[4] R. B. Witmer and J. M. Cork, The measurement of x-ray emission wave-length by means of the ruled grating, Phys. Rev. **42**, 743 (1932).

[5] B. Wang, C. Zhou, S. Wang, and J. Feng, Polarizing beam splitter of a deep-etched fused-silica grating, Opt. Lett. **32**, 1299 (2007).

[6] D. Fattal, J. Li, Z. Peng, M. Fiorentino, and R. G. Beausoleil, Flat dielectric grating reflectors with focusing abilities, Nat. Photonics **4**, 466 (2010).

[7] H. Kogelnik, Coupled wave theory for thick hologram grating, Bell Syst. Tech. J. **48**, 2909 (1969).

[8] L. Song, R. A. Lessard, and P. Galarneau, Diffraction efficiency of a thin amplitude-phase holographic grating: A convolution approach, J. Mod. Opt. **37**, 1319 (1990).

[9] N. Kukhtarev, G. Dovgalenko, G. C. Duree, Jr., G. Salamo, E. J. Sharp, B. A. Wechsler, and M. B. Klein, Single Beam Polarization Holographic Grating Recording, Phys. Rev. Lett. **71**, 4330 (1993).

[10] N. V. Kukhtarev, P. Buchhave, and S. F. Lyuksyutov, Optical and electric properties of dynamic holographic gratings with arbitrary contrast, Phys. Rev. A **55**, 3133 (1997).

[11] P. Wu, L. Wang, J. Xu, B. Zou, X. Gong, G. Zhang, G. Tang, W. Chen, and W. Huang, Transient biphotonic holographic grating in photoisomerizative azo materials, Phys. Rev. B **57**, 3874 (1998).

[12] M. B. Sobnack, W. C. Tan, N. P. Wanstall, T. W. Preist, and J. R. Sambles, Stationary Surface Plasmons on a Zero-Order Metal Grating, Phys. Rev. Lett. **80**, 5667 (1998).

[13] J. A. Porto, F. J. García-Vidal, and J. B. Pendry, Transmission Resonances on Metallic Gratings with Very Narrow Slits, Phys. Rev. Lett. **83**, 2845 (1999).

[14] W.-C. Tan, J. R. Sambles, and T. W. Preist, Double-period zero-order metal gratings as effective selective absorbers, Phys. Rev. B **61**, 13177 (2000).

[15] I. Freund, Nonlinear Diffraction, Phys. Rev. Lett. **21**, 1404 (1968).

[16] S. M. Saltiel, D. N. Neshev, R. Fischer, W. Krolikowski, A. Arie, and Y. S. Kivshar, Generation of Second-Harmonic Conical Waves via Nonlinear Bragg Diffraction, Phys. Rev. Lett. **100**, 103902 (2008).

[17] S. M. Saltiel, D. N. Neshev, W. Krolikowski, A. Arie, O. Bang, and Y. S. Kivshar, Multiorder nonlinear diffraction in frequency doubling processes, Opt. Lett. **34**, 848 (2009).

[18] S. M. Saltiel, D. N. Neshev, W. Krolikowski, N. Voloch-Bloch, A. Arie, O. Bang, and Y. S. Kivshar, Nonlinear Diffraction from a Virtual Beam, Phys. Rev. Lett. **104**, 083902 (2010).

[19] A. Shapira and A. Arie, Phase-matched nonlinear diffraction, Opt. Lett. **36**, 1933 (2011).

[20] D. Leykam, O. Bahat-Treidel, and A. S. Desyatnikov, Pseudospin and nonlinear conical diffraction in Lieb lattices, Phys. Rev. A **86**, 031805(R) (2012).

[21] Y. Chen, W. Dang, Y. Zheng, X. Chen, and X. Deng, Spatial modulation of second-harmonic generation via nonlinear Raman-Nath diffraction in an aperiodically poled lithium tantalite, Opt. Lett. **38**, 2298 (2013).

[22] X. Fang, D. Wei, Y. Wang, H. Wang, Y. Zhang, X. Hu, S. Zhu, and M. Xiao, Conical third-harmonic generation in a hexagonally poled $LiTaO_3$ crystal, Appl. Phys. Lett. **110**, 111105 (2017).

[23] C. Chen, C. Feng, and X. Hu, The modulation to nonlinear Raman-Nath diffraction via manipulating slopes of domain structures, J. Opt. **21**, 035501 (2019).

[24] M. Fleischhauer, A. Imamoglu, and J. P. Marangos, Electromagnetically induced transparency: Optics in coherent media, Rev. Mod. Phys. **77**, 633 (2005).

[25] H. Y. Ling, Y. Q. Li, and M. Xiao, Electromagnetically induced grating: Homogeneously broadened medium, Phys. Rev. A **57**, 1338 (1998).

[26] M. Mitsunaga and N. Imoto, Observation of an electromagnetically induced grating in cold sodium atoms, Phys. Rev. A **59**, 4773 (1999).

[27] G. C. Cardoso and J. W. R. Tabosa, Electromagnetically induced gratings in a degenerate open two-level system, Phys. Rev. A **65**, 033803 (2002).

[28] A. W. Brown and M. Xiao, All-optical switching and routing based on an electromagnetically induced absorption grating, Opt. Lett. **30**, 699 (2005).

[29] L. E. E. de Araujo, Electromagnetically induced phase grating, Opt. Lett. **35**, 977 (2010).

[30] S. A. Carvalho and L. E. E. de Araujo, Electromagnetically induced phase grating: A coupled-wave theory analysis, Opt. Express **19**, 1936 (2011).

[31] L. Zhao, W. Duan, and S. F. Yelin, All-optical beam control with high speed using image-induced blazed gratings in coherent media, Phys. Rev. A **82**, 013809 (2010).

[32] L. Zhao, W. Duan, and S. F. Yelin, Generation of tunable-volume transmission-holographic gratings at low light levels, Phys. Rev. A **84**, 033806 (2011).

[33] R. G. Wan, J. Kou, L. Jiang, Y. Jiang, and J. Y. Gao, Electromagnetically induced grating via enhanced nonlinear modulation by spontaneously generated coherence, Phys. Rev. A **83**, 033824 (2011).

[34] S. Q. Kuang, C. S. Jin, and C. Li, Gain-phase grating based on spatial modulation of active Raman gain in cold atoms, Phys. Rev. A **84**, 033831 (2011).

[35] L. Wang, F. Zhou, P. Hu, Y. Niu, and S. Gong, Two-dimensional electromagnetically induced cross-grating in a four-level tripod type atomic system, J. Phys. B: At. Mol. Opt. Phys. **47**, 225501 (2014).

[36] Y.-M. Liu, X.-D. Tian, X. Wang, D. Yan, and J.-H. Wu, Cooperative nonlinear grating sensitive to light intensity and photon correlation, Opt. Lett. **41**, 408 (2016).

[37] S. Asghar, S. Ziauddin, S. Qamar, and S. Qamar, Electromagnetically induced grating with Rydberg atoms, Phys. Rev. A **94**, 033823 (2016).

[38] V. G. Arkhipkin and S. A. Myslivets, One- and two-dimensional Raman-induced diffraction gratings in atomic media, Phys. Rev. A **98**, 013838 (2018).

[39] C. M. Bender and S. Boettcher, Real Spectra in Non-Hermitian Hamiltonians Having $\mathcal{PT}$ Symmetry, Phys. Rev. Lett. **80**, 5243 (1998).

[40] C. M. Bender, Making sense of non-Hermitian Hamiltonians, Rep. Prog. Phys. **70**, 947 (2007).

[41] V. V. Konotop, J. Yang, and D. A. Zezyulin, Nonlinear waves in $\mathcal{PT}$-symmetric systems, Rev. Mod. Phys. **88**, 035002 (2016).

[42] L. Feng, R. El-Ganainy, and L. Ge, Non-Hermitian photonics based on parity-time symmetry, Nat. Photonics **11**, 752 (2017).

[43] R. El-Ganainy, K. G. Makris, M. Khajavikhan, Z. H. Musslimani, S. Rotter, and D. N. Christodoulides, Non-Hermitian physics and $\mathcal{PT}$ symmetry, Nat. Phys. **14**, 11 (2018).

[44] S. Longhi, Bloch Oscillations in Complex Crystals with $\mathcal{PT}$ Symmetry, Phys. Rev. Lett. **103**, 123601 (2009).

[45] M. Wimmer, M. A. Miri, D. Christodoulides, and U. Peschel, Observation of Bloch oscillations in complex $\mathcal{PT}$-symmetric photonic lattices, Sci. Rep. **5**, 17760 (2015).

[46] H. Ramezani, T. Kottos, R. El-Ganainy, and D. N. Christodoulides, Unidirectional nonlinear $\mathcal{PT}$-symmetric optical structures, Phys. Rev. A **82**, 043803 (2010).

[47] L. Feng, M. Ayache, J. Huang, Y.-L. Xu, M.-H. Lu, Y.-F. Chen, Y. Fainman, and A. Scherer, Nonreciprocal light propagation in a silicon photonic circuit, Science **333**, 729 (2011).

[48] Z. Lin, H. Ramezani, T. Eichelkraut, T. Kottos, H. Cao, and D. N. Christodoulides, Unidirectional Invisibility Induced by $\mathcal{PT}$-Symmetric Periodic Structures, Phys. Rev. Lett. **106**, 213901 (2011).

[49] S. Longhi, $\mathcal{PT}$-symmetric laser absorber, Phys. Rev. A **82**, 031801(R) (2010).

[50] Y. D. Chong, L. Ge, and A. D. Stone, $\mathcal{PT}$-Symmetry Breaking and Laser-Absorber Modes in Optical Scattering Systems, Phys. Rev. Lett. **106**, 093902 (2011).

[51] Y. Sun, W. Tan, H. Li, J. Li, and H. Chen, Experimental Demonstration of a Coherent Perfect Absorber with $\mathcal{PT}$ Phase Transition, Phys. Rev. Lett. **112**, 143903 (2014).

[52] C. Hang, G. Huang, and V. V. Konotop, Tunable spectral singularities: coherent perfect absorber and laser in an atomic medium, New J. Phys. **18**, 085003 (2016).

[53] V. V. Konotop, V. S. Shchesnovich, and D. A. Zezyulin, Giant amplification of modes in parity-time symmetric waveguides, Phys. Lett. A **376**, 2750 (2012).

[54] L. Feng, Z. J. Wong, R. Ma, Y. Wang, and X. Zhang, Single-mode laser by parity-time symmetry breaking, Science **346**, 972 (2014).

[55] H. Hodaei, M.-A. Miri, M. Heinrich, D. N. Christodoulides, and M. Khajavikhan, Parity-time-symmetric microring lasers, Science **346**, 975 (2014).

[56] H. Jing, S. K. Özdemir, X.-Y. Lü, J. Zhang, L. Yang, and F. Nori, $\mathcal{PT}$-Symmetric Phonon Laser, Phys. Rev. Lett. **113**, 053604 (2014).

[57] J. Zhang, B. Peng, Ş. K. Özdemir, K. Pichler, D. O. Krimer, G. Zhao, F. Nori, Y.-X. Liu, S. Rotter, and L. Yang, A phonon laser operating at an exceptional point, Nat. Photonics **12**, 479 (2018).

[58] H. Xu, D. Mason, L. Jiang, and J. G. E. Harris, Topological energy transfer in an optomechanical system with exceptional points, Nature (London) **537**, 80 (2016).

[59] J. Doppler, A. A. Mailybaev, J. Böhm, U. Kuhl, A. Girschik, F. Libisch, T. J. Milburn, P. Rabl, N. Moiseyev, and S. Rotter, Dynamically encircling an exceptional point for asymmetric mode switching, Nature (London) **537**, 76 (2016).

[60] H. Hodaei, A. U. Hassan, S. Wittek, H. Garcia-Gracia, R. El-Ganainy, D. N. Christodoulides, and M. Khajavikhan, Enhanced sensitivity at higher-order exceptional points, Nature (London) **548**, 187 (2017).

[61] W. Chen, Ş. K. Özdemir, G. Zhao, J. Wiersig, and L. Yang, Exceptional points enhance sensing in an optical microcavity, Nature (London) **548**, 192 (2017).

[62] Y. Lai, Y. Lu, M. Suh, Z. Yuan, and K. Vahala, Observation of the exceptional-point-enhanced Sagnac effect, Nature (London) **576**, 65 (2019).

[63] L. Xiao, X. Zhan, Z. H. Bian, K. K. Wang, X. Zhang, X. P. Wang, J. Li, K. Mochizuki, D. Kim, N. Kawakami, W. Yi, H. Obuse, B. C. Sanders, and P. Xue, Observation of topological edge states in parity-time-symmetric quantum walks, Nat. Phys. **13**, 1117 (2017).

[64] L. Xiao, T. Deng, K. Wang, G. Zhu, Z. Wang, W. Yi, and P. Xue, Non-Hermitian bulk-boundary correspondence in quantum dynamics, Nat. Phys. **16**, 761 (2020).

[65] M. Naghiloo, M. Abbasi, Y. N. Joglekar, and K. W. Murch, Quantum state tomography across the exceptional point in a single dissipative qubit, Nat. Phys. **15**, 1232 (2019).
[66] C. Hang and G. Huang, Parity-time symmetry with coherent atomic gases, Adv. Phys. X **2**, 737 (2017).
[67] Z. Zhang, D. Ma, J. Sheng, Y. Zhang, Y. Zhang, and M. Xiao, Non-Hermitian optics in atomic systems, J. Phys. B: At. Mol. Opt. Phys. **51**, 072001 (2018).
[68] T. F. Gallagher, *Rydberg Atoms* (Cambridge University Press, Cambridge, 2008).
[69] J. D. Pritchard, K. J. Weatherill, and C. S. Adams, Nonlinear optics using cold Rydberg atoms, Annu. Rev. Cold At. Mol. **1**, 301 (2013).
[70] O. Firstenberg, C. S. Adams, and S. Hofferberth, Nonlinear quantum optics mediated by Rydberg interactions, J. Phys. B: At. Mol. Opt. Phys. **49**, 152003 (2016).
[71] C. Murray and T. Pohl, Quantum and nonlinear optics in strongly interacting atomic ensembles, in *Advances in Atomic, Molecular, and Optical Physics* (Academic Press, New York, 2016), Vol. 65, Chap. 7, pp. 321–372.
[72] Z. Bai, W. Li, and G. Huang, Stable single light bullets and vortices and their active control in cold Rydberg gases, Optica **6**, 309 (2019).
[73] J. Sinclair, D. Angulo, N. Lupu-Gladstein, K. Bonsma-Fisher, and A. M. Steinberg, Observation of a large, resonant, cross-Kerr nonlinearity in a free-space Rydberg gas, Phys. Rev. Research **1**, 033193 (2019).
[74] Y. Mu, L. Qin, Z. Shi, and G. Huang, Giant Kerr nonlinearities and magneto-optical rotations in a Rydberg-atom gas via double electromagnetically induced transparency, Phys. Rev. A **103**, 043709 (2021).
[75] Y. V. Kartashov, V. A. Vysloukh, V. V. Konotop, and L. Torner, Diffraction control in $\mathcal{PT}$-symmetric photonic lattices: From beam rectification to dynamic localization, Phys. Rev. A **93**, 013841 (2016).
[76] X.-Y. Zhu, Y.-L. Xu, Y. Zou, X.-C. Sun, C. He, M.-H. Lu, X.-P. Liu, and Y.-F. Chen, Asymmetric diffraction based on a passive parity-time grating, Appl. Phys. Lett. **109**, 111101 (2016).
[77] Y.-M. Liu, F. Gao, C.-H. Fan, and J.-H. Wu, Asymmetric light diffraction of an atomic grating with $\mathcal{PT}$ symmetry, Opt. Lett. **42**, 4283 (2017).
[78] T. Shui, W.-X. Yang, S. Liu, L. Li, and Z. Zhu, Asymmetric diffraction by atomic gratings with optical $\mathcal{PT}$ symmetry in the Raman-Nath regime, Phys. Rev. A **97**, 033819 (2018).
[79] C. Hang, W. Li, and G. Huang, Nonlinear light diffraction by electromagnetically induced gratings with $\mathcal{PT}$ symmetry in a Rydberg atomic gas, Phys. Rev. A **100**, 043807 (2019).
[80] Z. Bai and G. Huang, Enhanced third-order and fifth-order Kerr nonlinearities in a cold atomic system via Rydberg-Rydberg interaction, Opt. Express **24**, 4442 (2016).
[81] S. Mauger, J. Millen, and M. P. A. Jones, Spectroscopy of strontium Rydberg states using electromagnetically induced transparency, J. Phys. B: At., Mol. Opt. Phys. **40**, F319 (2007).
[82] The radius of the blockade sphere R_b is estimated by $R_b = (|C_6/\delta_{\rm EIT}|)^{1/6}$, with $\delta_{\rm EIT}$ the linewidth of EIT transmission spectrum (i.e., the width of EIT transparency window), calculated by $\delta_{\rm EIT} = |\Omega_c|^2/\gamma_{31}$ for $\Delta_3 = 0$ and $\delta_{\rm EIT} \approx |\Omega_c|^2/\Delta_3$ for $\Delta_3 \gg \gamma_{31}$.
[83] C. Hang, G. Huang, and V. V. Konotop, $\mathcal{PT}$ Symmetry with a System of Three-Level Atoms, Phys. Rev. Lett. **110**, 083604 (2013).
[84] R. W. Boyd, *Nonlinear Optics* (Academic Press, Amsterdam, 2003).
[85] This is different from conventional considerations of Bragg diffraction, where the light field can be approximated as a plane wave with infinitely large transverse width, and an oblique incidence is used [84].
[86] A. Jeffery and T. Kawahara, *Asymptotic Methods in Nonlinear Wave Theory* (Pitman, London, 1982).
[87] A. C. Newell and J. V. Moloney, *Nonlinear Optics* (Addison-Wesley, Redwood City, 1992).
[88] W. Królikowski, O. Bang, J. J. Rasmussen, and J. Wyller, Modulational instability in nonlocal nonlinear Kerr media, Phys. Rev. E **64**, 016612 (2001).
[89] W. Królikowski and O. Bang, Solitons in nonlocal nonlinear media: Exact solutions, Phys. Rev. E **63**, 016610 (2000).
[90] L. Karpa and M. Weitz, A Stern-Gerlach experiment for slow light, Nat. Phys. **2**, 332 (2006).
[91] Y. Guo, L. Zhou, L.-M. Kuang, and C. P. Sun, Magneto-optical Stern-Gerlach effect in an atomic ensemble, Phys. Rev. A **78**, 013833 (2008).